Contents lists available at ScienceDirect

Arabian Journal of Chemistry

journal homepage: www.ksu.edu.sa

Original article

Highly efficient remediation of chlorpyrifos and malachite green by an SBA-15 incorporated guar gum-*grafted*-poly (acrylic acid)/cobalt ferrite matrix for water purification

Mohammad Mehdi Salehi [a,1], Kimia Rajabi [a,1], Fereshte Hassanzadeh Afruzi [a,1], Fatemeh Ganjali [a,1], Ali Maleki [a,*], Ehsan Nazarzadeh Zare [b,*]

[a] *Catalysts and Organic Synthesis Research Laboratory, Department of Chemistry, Iran University of Science and Technology, Tehran 16846-13114, Iran*
[b] *School of Chemistry, Damghan University, Damghan 36716-45667, Iran*

ARTICLE INFO

Keywords:
Water treatment
Cationic dyes
Organophosphorus pesticides
Silica-based adsorbent
Kinetics
Isotherm

ABSTRACT

The Santa Barbara Amorphous-15-guar gum-*grafted*-poly (acrylic acid)/cobalt ferrite (SBA-15-GG-*g*-PAA/$CoFe_2O_4$) mesoporous adsorbent was prepared by graft copolymerization of acrylic acid (AA) onto guar gum (GG) in the Santa Barbara Amorphous-15 (SBA-15) substrate presence, followed by incorporating $CoFe_2O_4$ magnetic nanoparticles (MNPs). Diverse analyses were conducted to identify the prepared mesoporous adsorbent's chemical and morphological properties, thermal resistance, magnetic characteristics, surface area, and porosity. Based on the magnetic hysteresis loops, the mesoporous adsorbent rendered ferromagnetic behavior. According to TGA, it has char yields of 72 wt% at 800 °C and superparamagnetic behavior (Ms of 3.22 $emu.g^{-1}$). The crystalline structure and cubic phases of $CoFe_2O_4$ MNPs in the GG-*g*-PAA amorphous matrix were demonstrated by XRD. The $CoFe_2O_4$ MNP formation with partial aggregations onto smooth, nonporous, and regular surfaces of the GG was depicted by FESEM images. Also, the precisely-arranged hexagonal structure with cylindrical pores of SBA-15 was authenticated by FESEM images. Additionally, the SBA-15 substrate has increased the BET surface area of the prepared mesoporous adsorbent to 40.55 m^2/g, which is higher than the composite without SBA-15 mesoporous silica. Several experimental setups were used to evaluate the effectiveness of adsorption, including pH of the medium (4–9), Adsorbent dosage (0.003–0.02 g), Interaction time (1–25 min), and Initial pollutant concentration (50–400 mg/L). Using 0.003 g of mesoporous adsorbent at 25 °C, chlorpyrifos (CPF) and malachite green (MG) had maximum adsorption capacities (Qmax) of 909.1 mg/g and 1000.0 mg/g, respectively. In this study, the Langmuir isotherm model fitted the adsorption data perfectly with$R^2_{MG} = 0.9987$ and$R^2_{CPF} = 0.9994$, and the pseudo-second-order model explained the adsorption kinetics with $R^2_{MG} = 0.9644$ and $R^2_{CPF} = 0.9923$. MG and CPF adsorption to the SBA-15-GG-*g*-PAA/$CoFe_2O_4$ mesoporous adsorbent was successful due to hydrogen bonds, exchange interactions, diffusion, and entrapment in the hydrogel network. In addition to the three-dimensional structure, the mesoporous adsorbent has available adsorption sites for reactive molecules. The reusability of the SBA-15-GG-*g*-PAA/$CoFe_2O_4$ was perused and showed that the mesoporous adsorbent can be separated efficiently and retrieved in three sequential cycles without considerable diminution in the adsorption efficiency.

1. Introduction

Water asset deficiency could be a noteworthy issue that debilitates social order these days. Existing water capitals are lost due to displacement and advancement of businesses, improper management of municipal wastes, and lack of monitoring of water assets (Akter et al., 2022). In this respect, it appears inescapable not to use plant pesticides for horticulture to supply nourishment. In any case, this method discharges pesticides into the environment and causes their intemperate use (Beigi et al., 2023). Organophosphorus pesticides (OPPs) are

---

* Corresponding authors.
E-mail addresses: maleki@iust.ac.ir (A. Maleki), e.nazarzadeh@du.ac.ir, ehsan.nazarzadehzare@gmail.com (E. Nazarzadeh Zare).
[1] These authors contributed equally to this work.

https://doi.org/10.1016/j.arabjc.2024.105751
Received 26 December 2023; Accepted 21 March 2024

engineered pesticides among different pesticide sorts (Nandhini et al., 2021). One of the chlorinated organophosphate pesticides is chlorpyrifos (CPF). The CPF's long-term strength is ascribed to the physicochemical and structural properties. This pesticide is nonpolar and has low solubility in aquatic media, with an increasing solubility trend from aqueous to organic solvents (Beigi et al., 2023). Also, organic dyes demonstrate toxicity and low biodegradability, with carcinogenic effects on aquatics because of their stability and structural aromaticity (Boulahbal et al., 2022). MG is a triphenylmethane dye that is not allowed to be administrated as an animal medication in most parts of Europe, such as Germany, due to the teratogenic, carcinogenic, and mutagenic dangers that it causes to human health. Even though applying MG is illegal, it is broadly utilized as a parasiticide in aquatic nature and industries like health, food, etc. (Makhado et al., 2022). According to the mentioned risks for the environment and human health, water treatment from pesticide and organic dye contaminants is vital. Diverse physicochemical routes have been conducted to eliminate organic pollutants, including photocatalysis (Sedaghati et al., 2021), membrane filtration (Alfonso-Muniozguren et al., 2021), precipitation (Kim et al., 2021), degradation (Salehi et al., 2024), adsorption (Ansari et al., 2023; Hassanzadeh-Afruzi et al., 2022; Marjanian et al., 2021), etc. Despite the many advantages of these processes, they have many downsides when performing on large scales. For example, forming a concentrated slime is a procedure that takes energy and time, is costly, and has low effectiveness. Hence, adsorption is the most preferred pollutant elimination approach from aqueous media because of its operation inexpensiveness, improved efficiency, practicability, recyclability, and enhanced regeneration (Salehi et al., 2024).

Among various adsorbent systems, composites based on natural polymers are suggested for adsorption system design because of their accessibility, biodegradability, cost-effectiveness, and low toxicity (Beigi et al., 2023). The contaminant adsorption by the three-dimensional (3D) hydrogels, such as ghatti gum, arabic gum, cellulose, etc., improves the adsorption efficiency through the sorbent's functional groups and pollutants' molecules effective interactions (Nasrollahzadeh et al., 2021). The composite hydrogels are comprised of hydrophilic functional groups' grafting, viz., amine, amide, hydroxyl, carboxylic acid, and sulfuric acid to the polymer chain backbone and additives integration, such as metal–organic frameworks (MOFs), mesoporous silica materials, nanoparticles (NPs), etc. (Hajizadeh and Salehi, 2023; Salehi et al., 2023a). The biopolymer guar gum (GG) is obtained from the *Cyamopsis tetragonoloba* seed plant. Its components include mannose residues, galactose, and sugars (Khan et al., 2020a). The properties of GG make it a promising candidate for designing adsorbent systems (Kanwal et al., 2023). A wide range of applications can be gained from GG modification by various substances instead of the high solubility of GG in water and its sensitivity to salt media. Additionally, GG polymer strings' hydroxyl groups facilitate graft copolymerization, cross-linking, and hydrogen bonding to various materials (Saraf and Montazer, 2023). By cross-linking polymer strings, GG becomes more stable toward dissolution.

Incorporating nanomaterial additives improves surface area, reusability, and adsorption performance. Since recovering the NPs from the reaction mixture with the minimum NP loss is a significant parameter, adsorbent systems based on the magnetic composite evoke the scientists' attention (Hassanzadeh-Afruzi et al., 2023b). In this regard, magnetic composites have been applied as an appropriate system for decontaminating aqueous media (Nakhjiri et al., 2021). Some other broadly applied adsorbents are bentonite, metal oxide, metal hydroxides, clays, zeolites, biological materials, etc. (Kobayashi et al., 2020; Najafi et al., 2021; Wang et al., 2020; Yadav et al., 2021). Nonetheless, their serious disadvantages include hard retrievability, ineffective adsorption procedure, and loose interactions between adsorbent and metal ions (Wang et al., 2021). Organic-inorganic hybrid adsorbents (Gil et al., 2021), modified carbon-based NPs (Duan et al., 2020), chitosan (Upadhyay et al., 2021), CNTs (Bassyouni et al., 2020), and nanoporous materials (Atoub et al., 2020) are used to overcome these drawbacks. SBA-15 is a siliceous nanomaterial employed in adsorption applications due to its mesoporosity, improved surface area, and substantial hydrothermal resistance, whose surface can be conveniently functionalized (Dolatyari et al., 2019; Dolatyari et al., 2018). SBA-15 renders hexagonal and cylindric pores with pore sizes of 5–30 nm and wall pores' thickness of 3.1–6.4 nm (Dulski et al., 2020; Gámez et al., 2020), which are larger than MCM-41, another silica material, makes a facile diffusion of reactant molecule into the framework (Farrag, 2022). The applicability of SBA-15 has been reported as a catalyst (Farajzadeh et al., 2020), as an adsorbent in wastewater treatment (Dindar et al., 2016), drug delivery (Alazzawi et al., 2021), etc. For the SBA-15 materials' performance improvement, their surface functionalization is primarily exerted by approaches including co-condensation and post-grafting. In the chemical functionalization of SBA-15, which has well-ordered pores, more active sites are available for efficient interaction with pollutants (Dolatyari et al., 2017a; Dolatyari et al., 2017b).

In a study, 2-acetylthiophene-derived Schiff's bases were functionalized with SBA-15 to form A-SBA-15. A-SBA-15 has the highest adsorption capacity (56.7 mg/g) for Cr (III) removal (Wu et al., 2020). Another study was performed by Tzong-Horng Liou et al. on the modification of silica composites (SBA-15 and 3-aminopropyltriethoxysilane (APTES) and SBA-15 and pentaethylenehexamine (PEHA)). SBA-15/APTES showed ultrafast removal of tannic acid (TA) with a 98.61 % removal rate at 15 min. In contrast, SBA-15/APTES and SBA-15/PEHA showed maximum adsorption capacity for TA at 485.18 and 413.33 mg/g, respectively (Liou et al., 2022). Fenglei Liu et al. reported that Fe_3O_4@SBA-15-PDA/HBP-NH_2 adsorbent (Fe_3O_4@SBA-15-PDA/HBP-NH_2) was fabricated with a magnetic amine-functionalized mesoporous silica surface. As a result, under optimal water environment conditions, Fe_3O_4@SBA-15-PDA/HBP-NH_2 could adsorb U(VI) and Cr(VI) with 77.4 mg/g and 66.5 mg/g adsorption capacities, respectively (Liu et al., 2022). Mehdi Sadeghi et al. prepared a PPI@SBA-15/ZIF-8 super-adsorbent for the adsorption of Penicillin G from an aqueous medium. According to the results, Langmuir ($R^2 = 0.9944$, $Q_m = 400$ mg/g) for the adsorption isotherm and pseudo-second-order ($R^2 = 0.9905$) for the kinetics studied showed the best fit (Sadeghi et al., 2023).

Heavy metal ions (HMIs) and antibiotics' adsorption from water have been the focus of most existing studies. However, they're not very practical because of their poor adsorption capacity and slow kinetics. In contrast, natural polymers have good performance, very low cost, and are biodegradable. In this situation, there's a need for sustainable bio-based materials that can match the adsorption efficiency of natural polymers. GG is commonly used as a thickener and stabilizer in food, pharmaceuticals, and cosmetics due to its binding and emulsifying properties, but it isn't used much for water treatment. This grafting process would help the nanoparticles and mesopores adsorb more pollutants and reduce the environmental impact of water treatment. Further research is needed to develop improved grafting techniques and bio-based materials for environmental remediation. In a recent report, the SBA-15 functionalization was exerted by polyamidoamine through the grafting route for contaminant elimination from water (Zanele et al., 2021).

To sum up, for efficient CPF and MG removal from water, a mesoporous adsorbent was suggested via graft copolymerization. In this regard, the PAA graft copolymerization onto GG was accomplished on the SBA-15 substrate and in $CoFe_2O_4$ MNPs' presence. The ammonium persulfate (APS) and Borax were used as a polymerization radical initiator and a chemical cross-linking agent. The SBA-15-GG-*g*-PAA/$CoFe_2O_4$ mesoporous adsorbent with various functional groups and upgraded porosity can efficiently adsorb CPF and MG from water with an enhanced adsorption performance.

2. Experimental segment

2.1. Materials

High purity materials have been supplied by Sigma-Aldrich and used, such as $Fe(NO_3)_3{\cdot}9H_2O$ (≥98.0 %), $CoCl_2{\cdot}6H_2O$ (98.0 %), NaOH (≥98.0 %, pellets (anhydrous)), $(NH_4)_2S_2O_8$ ((APS) ≥ 98.0 %), Tetraethyl orthosilicate (TEOS) (98.0 %), Ethanol (95.0 %), HCl (37.0 %), Borax (BioUltra, anhydrous ≥ 99.0 %), Acrylic acid (Anhydrous, contains 200.0 mg/L MEHQ as an inhibitor, 99.0 %), Pluronic p-123 (Sigma-Aldrich, CAS No.: 9003–11–6), Guar gum (Sigma-Aldrich, CAS No.: 9000–30–0).

2.2. Devices

Different spectroscopic and microscopic approaches have been applied, including FTIR (Shimadzu, FTIR-8400S model, Japan), XRD (DRON-8, Saint-Petersburg, Russia), EDX (VEGA-TESCAN-XMU model, Czech Republic), BET (BET, Micrometics ASAP2020, USA), VSM (Meghnatis, Daneshpajooh Company, Iran), TGA (BAHR-STA 504 apparatus, Germany), pH meter (PHS 3C), UV–Visible spectrometer (Shimadzu, 2550, 220 V, Japan), FESEM (KYKY-EM8000F, China, and ZEISS SIGMA, Germany), TEM (Carl Zeiss-EM10C-100Kv-Germany), Autoclave (ReyhanTeb 2KW-220 V-Iran), Filter paper (Whatman (grade 602 h, Particle retention < 2 μm)), Oven (Genlab Ltd, UK), Freeze Drying (KASSEL Machinery (Zhejiang) Co., Ltd, China), Thermometer (Fluke (572–2 infrared), China), Zeta potential (Bruker, D8 advance, USA).

2.3. Preparation of the SBA-15-GG-g-PAA/$CoFe_2O_4$ magnetic mesoporous adsorbent

2.3.1. Preparation of the $CoFe_2O_4$ MNPs

The $CoFe_2O_4$ MNPs were prepared via a facile co-precipitation procedure (Fig. 1a). In this regard, 3.23 g (8.0 mmol) of the $Fe(NO_3)_3{\cdot}9H_2O$, 1.09 g (4.0 mmol) $CoCl_2{\cdot}6H_2O$, and 25.0 mL distilled water (d.w.) was transferred into a 250.0 mL two-neck flask and stirred for 1 h at 80 °C under an N_2 atmosphere. Afterward, 25.0 mL of the NaOH (4 M) solution was added gently, and the temperature was raised to 90 °C. The reaction was continued for 1 h to form $CoFe_2O_4$ MNPs. After cooling, the black sediment was magnetically isolated and rinsed with d.w. 10 to 15 times to attain a neutral pH. Ultimately, the obtained $CoFe_2O_4$ MNPs were dried at 60–65 °C (12 h) (Vishwas et al., 2022).

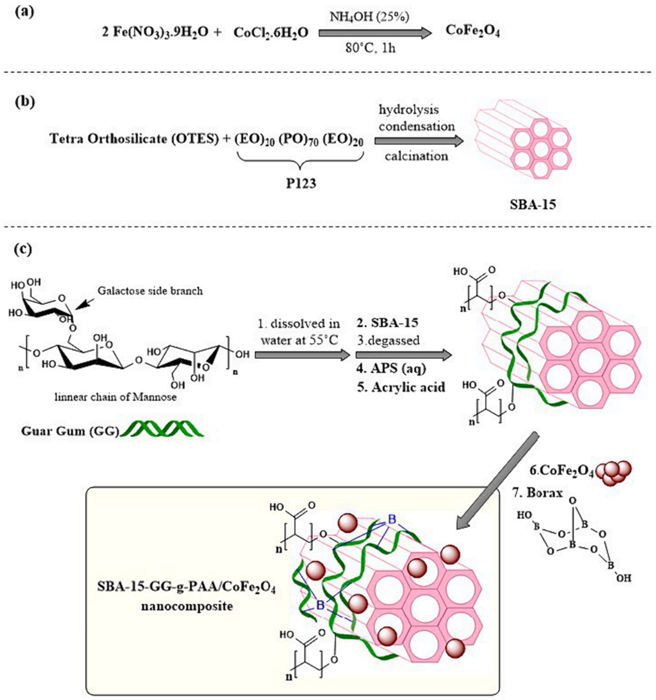

Fig. 1. The scheme of the preparation route of the magnetic SBA-15-GG-*g*-PAA/$CoFe_2O_4$ mesoporous adsorbent.

2.3.2. Preparation of the SBA-15

The SBA-15 in this study was prepared based on the hydrothermal approach reported in the previous studies (Fig. 1b) (Hassanzadeh-Afruzi et al., 2022). For this purpose, in a 250.0 mL flask, the P123 surfactant (3.5 g) as a structural template was dissolved in 120 mL hydrochloric acid (HCl) with a 1.4 M concentration and stirred for 24 h (40 °C). Then, 8.0 mL of tetraethyl orthosilicate (TEOS) was poured into the mixture under stirring for another 24 h at 40 °C to complete the silica source hydrolysis. The reaction mixture was poured into a Teflon-lined stainless-steel autoclave at 150 °C for 24 h. After the desired time, it was rinsed 15 times with d.w. under a vacuum pump and dried at an ambient temperature. Eventually, the resulting white powder was calcinated at 500 °C for 4 h at a heating rate of 2.3 °C/min for the surfactant template elimination, creating a mesoporous SBA-15 with a large range of the ordered channels.

2.3.3. Preparation of the GG-g-PAA/$CoFe_2O_4$

GG-*g*-PAA was synthesized by grafting AA on GG through free radical polymerization in an aqueous system using APS as the initiator (Fig. 1c) (Salehi et al., 2023b). The reaction steps are as follows. First, 0.5 g of GG was dissolved in a 250.0 mL two-neck round bottom flask containing 25.0 mL d.w. at 50 °C and degassed with nitrogen as inert gas for 10 min. The AA monomer (0.114 g) in 25.0 mL of d.w. was added gently to the reaction mixture and stirred at 60 °C. After 10 min, APS (0.23 g (1 mmol)) in 10 mL)) was poured into the solution dropwise under an N_2 atmosphere. Then, the as-prepared $CoFe_2O_4$ MNPs (0.75 g) in 15.0 mL of d.w. were sonicated for better dispersion. After 20 min, the dispersed $CoFe_2O_4$ MNPs were added to the reaction solution dropwise. At last, after 4 h at 60 °C, all the flask contents were added to a large beaker containing soluble Borax ($Na_2[B_4O_5(OH)_4]{\cdot}8H_2O$) as a chemical cross-linker. After 1 h, ethanol was added to the solution to form the desired hydrogel. The resultant was washed with ethanol and d.w. to eliminate the residual Borax and unreacted reagents and dried in a freeze-dryer.

2.3.4. Preparation of the magnetic SBA-15-GG-g-PAA/$CoFe_2O_4$ mesoporous adsorbent

Initially, GG (0.5 g) was dissolved in 25.0 mL d.w. in a two-neck flask (250.0 mL) at 50 °C. Afterward, GG was added to the SBA-15-containing flask (0.5 g) in d.w. (40.0 mL) and stirred for 1 h (25 °C). Then, it was degassed with nitrogen for 10 min since oxygen must be removed to proceed with radical polymerization, and an inert gas such as nitrogen must be used. Next, the AA (0.114 g) in d.w. (25.0 mL) was added to the solution dropwise at 60 °C, and after 40 min, APS (0.23 g (1 mmol) in 10 mL) was moved gently to the solution under an N_2 atmosphere. The as-prepared $CoFe_2O_4$ MNPs (0.75 g) were dispersed in 15.0 mL d.w. by sonication for 20 min and then added to the reaction solution dropwise. Ultimately, after stirring for 4 h at 60 °C, all the flask contents were added to a large beaker containing soluble Borax. Then, ethanol was added to the solution to form the desired hydrogel. The resultant was washed with ethanol and d.w. to eliminate the residual Borax and unreacted reagents, and finally, it was freeze-dried.

2.3.5. Obtaining real samples

Eight real water samples were collected from the Gilan, Gorgan, and Khozestan provinces in northern and southern Iran. Samples were collected from Goharroud, Zarjoub, Gorgan, and Karun rivers. A pre-cleaned amber retention container was used to store all samples. The samples were filtered using Whatman filter paper of 602 h grade, particle size 2 nm. A subsequent step was to store the samples at 25 °C until they were analyzed accordingly (Hassani et al., 2023; Salehi et al., 2024).

2.4. General procedures

We rigorously designed the experimental procedure to ensure that the results obtained are reliable and reproducible. A UV–Vis diffuse reflectance spectroscopy measurement was conducted in triplicate, and the data was averaged to minimize variability. For establishing a reference point for comparison, baseline UV–Vis measurements were taken before introducing the mesoporous adsorbent, CPF, and MG, into the system, using linear regression equations $y = 0.1 + 0.065\ x$, $R^2 = 0.99$ and $y = 0.1221 + 0.0233\ x$, $R^2 = 0.9915$, respectively (Fig. S1 and S2). MG and CPF were quantified accurately with these calibration curves in subsequent experiments. During the experiment, 0.003–0.02 g of SBA-15-GG-*g*-PAA/$CoFe_2O_4$ mesoporous adsorbent was mixed with 10.0 mL of CPF and MG solutions. In order to investigate how pH affects the adsorption process, 0.1 M NaOH and HCl solutions were used to adjust the pH of the solution within the range of 4 to 9, along with calculating the resistance of the preparation solution containing NaOH and HCl on pages S4 and S5, SI. The pH adjustment was crucial as it can significantly affect the surface charge of the SBA-15-GG-g-PAA/$CoFe_2O_4$ mesoporous adsorbent and their interaction with CPF and MG species. The solution was stirred for 1–25 min using a magnetic stirrer to ensure uniform distribution and thoroughly mix the components. A 25–250 mg/L concentration is recommended as an initial concentration (pages S6 and S7, SI). As a result of this mixing step, the mixture of SBA-15-GG-*g*-PAA/$CoFe_2O_4$ mesoporous adsorbent and CPF and MG molecules was more efficient, facilitating adsorption. Using the stirring process, we improved the adsorption efficiency and effectiveness of the SBA-15-GG-*g*-PAA/$CoFe_2O_4$ mesoporous adsorbent as a potential adsorbent material by maximizing contact between the mesoporous adsorbent surface and the adsorbate molecules. We aimed to determine the adsorption behavior of SBA-15-GG-*g*-PAA/$CoFe_2O_4$ mesoporous adsorbent toward CPF and MG by using this systematic and meticulous experimental procedure, thereby providing valuable insights into how SBA-15-GG-*g*-PAA/$CoFe_2O_4$ mesoporous adsorbent might be used in environmental remediation as an efficient adsorbent (Ebrahimpour et al., 2022; Salehi et al., 2024).

2.5. Batch adsorption studies

The capability of the prepared magnetic SBA-15-GG-*g*-PAA/$CoFe_2O_4$ mesoporous adsorbent in CPF and MG adsorption from the aqueous environment has been perused by adsorption experiments. The CPF and MG calibration curves have been represented in Fig. S1 and S2. For adsorption capacity calculations, the variable factors have been investigated, like the solution pH, the adsorbent dosage, the contact time of the reaction, and the contaminant's (i.e., CPF and MG) initial concentration. Different factors were inspected to inquire into the optimum adsorption conditions. The 0.1 M of HCl and 0.1 M of NaOH solution were utilized to regulate the pH in the 4–9 range, and the SBA-15-GG-*g*-PAA/$CoFe_2O_4$ mesoporous adsorbent (3.0–20.0 mg) was employed in contact time of 1–25 min, and the CPF and MG primary concentration were 50.0–400.0 mg/L. Additionally, the isotherms of adsorption were determined by comparing the experimental results and Freundlich and Langmuir models. Besides, the investigation of adsorption kinetics was exerted by pseudo-first-order and pseudo-second-order models. The CPF and MG concentrations were specified via UV–Vis spectrophotometry. Furthermore, the removal efficiency (Eq.1) and adsorption capacity (Eq.2) of the SBA-15-GG-g-PAA/$CoFe_2O_4$ mesoporous adsorbent are calculated for CPF and MG pollutants (Salehi et al., 2024).

$$\mathrm{R}\ (\%) = \frac{(C_0 - C_i)}{C_0} \times 100 \tag{1}$$

$$\mathrm{Qe} = \frac{(C_0 - C_i) \times V}{m} \tag{2}$$

Where C_i and Ce, with similar "mg/L" units, are the primary concentration and an equilibrium concentration of the CPF and MG in water, respectively. V (L) represents the volume of the solution, and m (g) stands for the weight of magnetic SBA-15-GG-*g*-PAA/$CoFe_2O_4$ mesoporous adsorbent.

2.6. Regeneration and retrievability

The reusability test was performed to understand the magnetic SBA-15-GG-*g*-PAA/$CoFe_2O_4$ adsorbent's regeneration feasibility and the expenses related to the water treatment process. In the current work, three successive retrievability cycles at optimum conditions were examined to evaluate the magnetic SBA-15-GG-*g*-PAA/$CoFe_2O_4$ mesoporous adsorbent's reusability after CPF and MG adsorption. The CPF adsorption test was carried out using the following steps. After the CPF adsorption in optimum conditions by magnetic SBA-15-GG-*g*-PAA/$CoFe_2O_4$ adsorbent in the solution volume of 10.0 mL, an adsorbent amount of 0.003 g, contact time of 20 min, pH = 7, and primary concentration of 400.0 mg/L at 25 °C, the mesoporous adsorbent was transferred into a beaker containing ethanol (25.0 mL) and stirred for 3 h at an ambient temperature. Besides, in the case of MG adsorption test, after the adsorption of MG by SBA-15-GG-*g*-PAA/$CoFe_2O_4$ mesoporous adsorbent in optimal conditions (the volume of solutions: 10.0 mL, adsorbent dose: 0.003 g, adsorption reaction time: 15 min, pH = 9, primary concentration: 400.0 mg/L, at 25 °C), the mesoporous adsorbent was stirred in a beaker containing HCl solution (0.1 M) at 25 °C. The mesoporous adsorbent was magnetically separated after desorption. The amount of released CPF and MG into the beaker was then perused by UV–Vis spectrophotometry. The Eq.3 demonstrates the mesoporous adsorbent desorption percentage (D%).

$$\mathrm{D}\ (\%) = \frac{A}{B} \times 100 \tag{3}$$

where A and B, with similar "mg" units, represent the desorbed quantity of the pollutants in the elution medium, the adsorbed quantity of the contaminants by magnetic SBA-15-GG-*g*-PAA/$CoFe_2O_4$ mesoporous adsorbent.

3. Results and discussion

According to the SBA-15-GG-*g*-PAA/$CoFe_2O_4$ mesoporous adsorbent preparation process (such as $CoFe_2O_4$ MNPs, SBA-15, GG-*g*-PAA/$CoFe_2O_4$, and SBA-15-GG-*g*-PAA/$CoFe_2O_4$ mesoporous adsorbent), various analyses were exerted to clarify mesoporous adsorbent's different characteristics, that will be debated.

3.1. Preparation of the SBA-15-GG-g-PAA/$CoFe_2O_4$ mesoporous adsorbent

The SBA-15-GG-*g*-PAA/$CoFe_2O_4$ mesoporous adsorbent was prepared and employed to eliminate CPF and MG from aqueous media. Fig. 1 exhibits the preparation steps of the SBA-15-GG-*g*-PAA/$CoFe_2O_4$ mesoporous adsorbent. Although using GG is beneficial, bare GG is undesirable because of the low adsorption capacity and inadequate thermal stability. Hence, to prevail over this issue, a novel hydrogel nanocomposite based on GG was designed by graft copolymerization with AA through a chemical bonding in the SBA-15 presence with mesoporous structure as a substrate. The SBA-15 and $CoFe_2O_4$ MNPs were incorporated into the polymeric matrix through the hydrogen bond network (Gihar et al., 2021). The APS was the polymerization radical initiator, and Borax played the role of a chemical cross-linking agent to create a three-dimensional (3D) hydrogel. Also, the $CoFe_2O_4$ MNPs with ferromagnetic behavior were incorporated into the composite to aid facile magnetic separation and enhance recyclability. Therefore, the prepared mesoporous adsorbent renders improved structural stability in water, has a high surface area, and has diverse functional groups that provide a favored functionality in CPF and MG elimination.

3.2. Characterization of the prepared SBA-15-GG-g-PAA/$CoFe_2O_4$ mesoporous adsorbent

3.2.1. Fourier transform infrared spectroscopy

FTIR spectroscopy was applied to verify the step-by-step preparation of SBA-15-GG-*g*-PAA/$CoFe_2O_4$ mesoporous adsorbent and confirm functional groups. Fig. 2a shows two vibrational bands at ca. 450 cm^{-1} to 600 cm^{-1}, which are attributed to the formation of the $CoFe_2O_4$ spinel structure. The strong peak observed at 587.93 cm^{-1} is related to the vibrational frequency of Fe − O. The small peak at ca. 450 cm^{-1} is assigned to the Co − O vibration frequency in the ferrite structure. $CoFe_2O_4$ is an inverted spinel ferrite, while Fe^{3+} and Co^{2+} ions occupy tetrahedral and octahedral sites, respectively (Ahmadi et al., 2020). The second spectrum (Fig. 2b) is related to the pure substance of GG. Four distinctive absorption peaks exist in this spectrum, similar to the recorded reports of the chemical structure of GG in other articles (Dutta et al., 2017). Some indicative bands are exhibited at 3430 cm^{-1}, 2922 cm^{-1}, and 1023 cm^{-1} due to the stretching vibration of O − H, C − H, and C − O–H groups, as well as the absorption band of C − O − C in the range of 1166 cm^{-1} (Dutta et al., 2017). The spectrum shown in Fig. 2c is related to the FTIR analysis of SBA-15. This silica network has characteristic absorption bands at 3500 cm^{-1} related to the O − H bond's stretching vibration of silanol groups and the remaining adsorbed water molecules in the sample. Symmetric stretching and bending vibration (Si − O − Si) appear at 1082 and 470 cm^{-1}, respectively. The peak at ca. 802 cm^{-1} corresponds to Si − OH, characteristic of mesoporous silica (Dolatyari et al., 2016a; Yousofvand et al., 2018). Fig. 2d shows the spectrum of the GG-*g*-PAA/$CoFe_2O_4$, which has a series of absorption bands different from the final composite. The formed glycosidic bonds appeared in 1100 cm^{-1}. From 1600 cm^{-1} to 1700 cm^{-1} is related to PAA grafted with GG. The stretching vibrations of carbonyl in carboxylic acid and other bonds confirm the formation of a graft copolymer. Also, a peak at 587 cm^{-1} demonstrates the $CoFe_2O_4$ MNPs. Ultimately, In the FT-IR of the SBA-15-GG-*g*-PAA/$CoFe_2O_4$, Fig. 2e, there are significant absorption bands at 1000 cm^{-1} related to the Si-O-Si stretching bond. Compared to GG -*g*-PAA/$CoFe_2O_4$, the peaks become more intense and look similar to SBA-15. This mesoporous adsorbent is a combination of distinctive absorption bands that confirm this structure. At 3400 cm^{-1}, there is a strong band related to OH, and in about 1600 cm^{-1} to 1700 cm^{-1}, the absorption band is associated with grafted with GG, and in the 580 cm^{-1}, the peak is ascribed to Fe − O.

3.2.2. Energy dispersive X-ray spectroscopy

Identification of constituent elements in the prepared samples, i.e., $CoFe_2O_4$, GG, SBA-15, GG-*g*-PAA/$CoFe_2O_4$, and SBA-15-GG-*g*-PAA/$CoFe_2O_4$ mesoporous adsorbent was done by EDX analysis. Fig. 3a shows the EDX diagram of $CoFe_2O_4$ MNPs. The peaks related to Co, Fe, and O, the constituent elements of $CoFe_2O_4$, are displayed well and with high intensity, indicating the formation of $CoFe_2O_4$ MNPs. Also, EDX spectra in Fig. 3b and Fig. 3c are ascribed to GG with C and O elements and SBA-15 with Si and O elements, respectively. In Fig. 3d, the GG-*g*-PAA/$CoFe_2O_4$ has four indicative peaks related to Co, C, O, and Fe elements, from which the graft copolymerization of PAA onto GG is concluded. However, the elemental analysis results of SBA-15-GG-*g*-PAA/$CoFe_2O_4$ mesoporous adsorbent show the Si, Co, C, O, and Fe elements with strong peaks. Besides, the presence of Si peak confirms the presence of SBA-15, which shows that the graft copolymerization of PAA onto GG has been accomplished in the SBA-15 substrate presence.

3.2.3. Electron microscopy

FESEM imaging has perused the surface morphology, particle aggregation, and particle size distribution. The $CoFe_2O_4$, GG, SBA-15, GG-*g*-PAA/$CoFe_2O_4$, and SBA-15-GG-*g*-PAA/$CoFe_2O_4$ mesoporous adsorbent FESEM images are presented in Fig. 4a-e. In Fig. 4a, the structure of $CoFe_2O_4$ MNPs can be observed well witnessed. However, it seems that they are aggregated in some parts. Fig. 4b is related to the GG FESEM image, which shows a relatively smooth and regular surface without porosity. Besides, Fig. 4c belongs to the SBA-15 structure, showing a

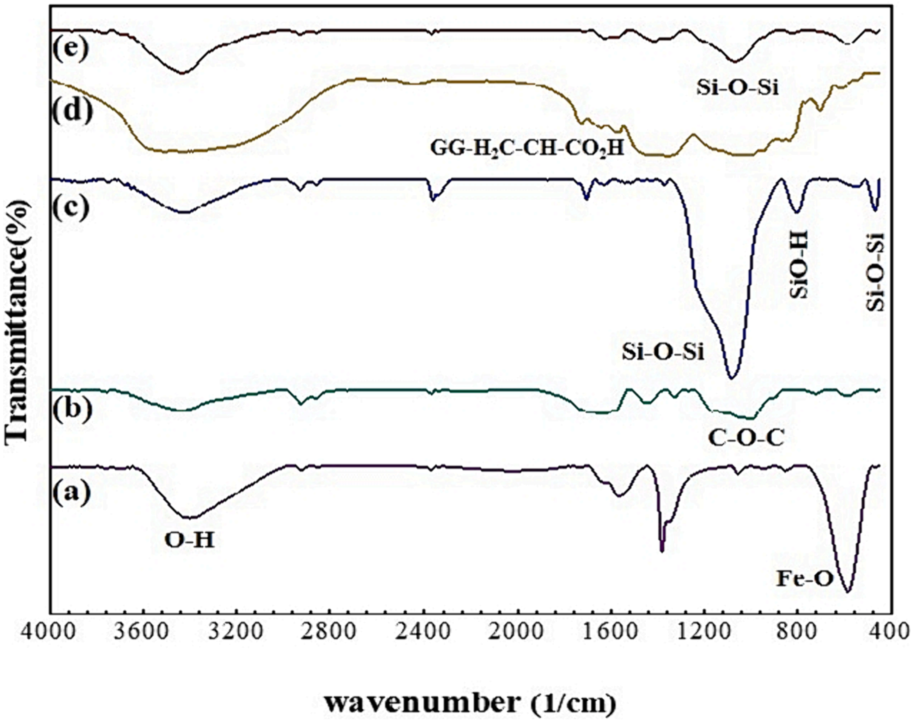

Fig. 2. The FTIR spectra of (a) $CoFe_2O_4$, (b) GG, (c) SBA-15, (d) GG-*g*-PAA/$CoFe_2O_4$, and (e) SBA-15-GG-*g*-PAA/$CoFe_2O_4$ mesoporous adsorbent.

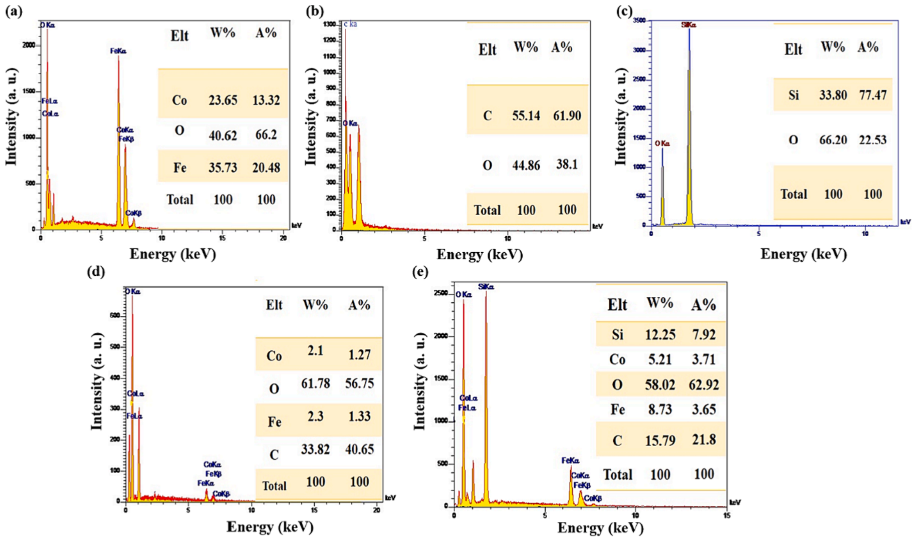

Fig. 3. The EDX analysis of (a) $CoFe_2O_4$, (b) GG, (c) SBA-15, (d) GG-*g*-PAA/$CoFe_2O_4$, and (e) SBA-15-GG-*g*-PAA/$CoFe_2O_4$ mesoporous adsorbent.

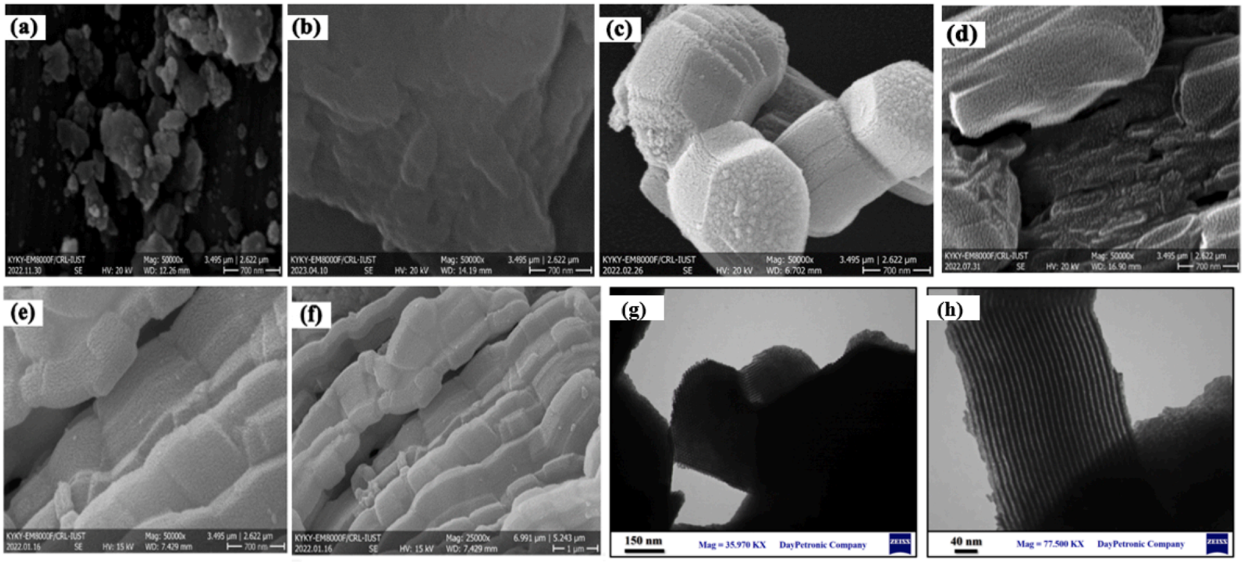

Fig. 4. The FESEM images of (a) $CoFe_2O_4$, (b) GG, (c) SBA-15, (d) GG-*g*-PAA/$CoFe_2O_4$, (e,f) SBA-15-GG-*g*-PAA/$CoFe_2O_4$ mesoporous adsorbent, and TEM images of (g,h) SBA-15-GG-*g*-PAA/$CoFe_2O_4$ mesoporous adsorbent.

well-ordered hexagonal structure and cylindrical channels. The image of GG-*g*-PAA/$CoFe_2O_4$ in Fig. 4d showed the morphology of GG after graft copolymerization with AA. The swollen spherical structures observed on the smooth surface are attributed to homogeneous graft copolymerizing AA onto the GG and cross-linking reactions. In the last two images (Fig. 4e,f), the modified SBA-15-GG-*g*-PAA/$CoFe_2O_4$ mesoporous adsorbent has a series of surface ridges, and this change in structure compared to the individual SBA-15 is due to the graft copolymerization reaction onto GG natural polymer chain which exerted on the SBA-15 substrate. In addition, in Fig. 4e, the presence of $CoFe_2O_4$ MNPs around the modified SBA-15 can be observed. TEM images were used to characterize magnetic mesoporous adsorbent in greater detail to confirm the prepared mesoporous adsorbent morphology. In Fig. 4 g,h, SBA-15-GG-*g*-PAA/$CoFe_2O_4$ mesoporous adsorbent shows highly arranged pores with 2D hexagonal morphology. By forming $CoFe_2O_4$ *ex-situ* and modifying the mesoporous adsorbents following, some segments of the mesostructured SBA-15 were concealed (Dolatyari et al., 2016b; Rafe et al., 2024).

3.2.4. *Vibrating-sample magnetometer study*

VSM study evaluated the magnetic features of the $CoFe_2O_4$, GG-*g*-PAA/$CoFe_2O_4$, and SBA-15-GG-*g*-PAA/$CoFe_2O_4$ mesoporous adsorbent. The VSM diagram is demonstrated in Fig. 5 with the − 10 to + 10 kOe magnetic field range. The magnetic saturation of $CoFe_2O_4$ is 46.01 emu g^{-1}. It has a hysteresis loop, indicating that $CoFe_2O_4$ MNPs are ferromagnetic materials (Nguyen and Huynh, 2014). The GG-*g*-PAA/$CoFe_2O_4$ and magnetic SBA-15-GG-*g*-PAA/$CoFe_2O_4$ mesoporous adsorbent exhibited magnetic saturation values of 6.146 and 3.22 emu g^{-1}, respectively. The hysteresis loop is still visible and preserved due to the $CoFe_2O_4$ magnetic component. In general, the decrease in magnetism was attributed to the non-magnetic components of the nanocomposite, i.e., GG grafted PAA and SBA-15 as a non-magnetic mineral that caused the overall magnetism decrease. Incorporating $CoFe_2O_4$ MNPs embedded in/onto the channels of SBA-15 and the GG-*g*-PAA hydrogel has caused magnetic properties. As a result, the magnetic property of the material is due to the presence of $CoFe_2O_4$ MNPs, which are magnetically isolated by ease.

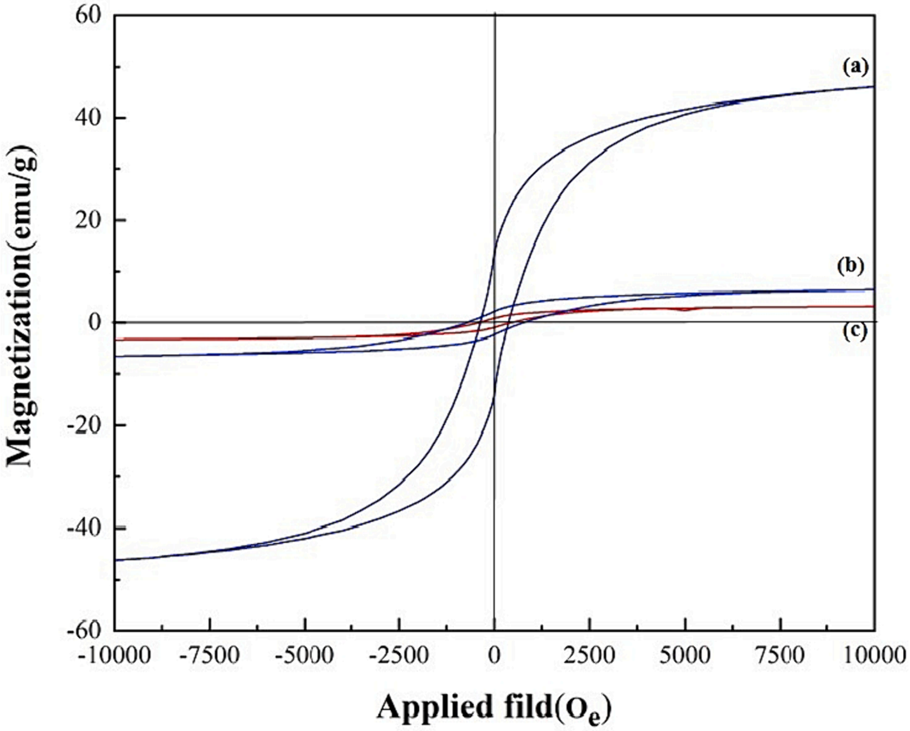

Fig. 5. The VSM analysis of (a) $CoFe_2O_4$, (b) GG-*g*-PAA/$CoFe_2O_4$, and (c) SBA-15-GG-*g*-PAA/$CoFe_2O_4$ mesoporous adsorbent.

3.2.5. *Thermogravimetric analysis*

The thermal resistance of the SBA-15, $CoFe_2O_4$, and SBA-15-GG-*g*-PAA/$CoFe_2O_4$ mesoporous adsorbent has been investigated and represented in Fig. 6. SBA-15 is a completely inorganic material with no organic parts and high thermal stability. Based on the thermogram of SBA-15, it is very stable to the temperature increase and showed almost no weight loss up to 800 °C (Hassanzadeh-Afruzi et al., 2022). $CoFe_2O_4$ MNPs are minerals that lose only 6 % of their weight up to 800 °C. The first stage of weight loss (2 %) occurred at a temperature below 130 °C related to the loss of entrapped water, and the following 4 % weight loss in the range of 130 °C to 800 °C is the result of decomposition of nitrate groups or deformation of ferrite phases (Sivagurunathan and Gibin, 2016). The thermogram of the SBA-15-GG-*g*-PAA/$CoFe_2O_4$ mesoporous adsorbent shows a greater weight loss than the thermogram of $CoFe_2O_4$ MNPs and SBA-15, resulting in lower thermal resistance. The decrease in the TGA curve under 200 °C is generally attributed to the entrapped water or solvent loss, which is about 15 %. The observed weight loss from 200 °C to 400 °C is associated with the functional groups attached to GG. Besides, the weight loss of 9 % from 400 °C to 500 °C is related to the GG natural polymer. Natural polymers usually decompose up to 500 °C. The functional groups are separated first, then the linked PAA with GG, and the glycosidic bonds that connect this biopolymer are broken. Finally, the organic part is decomposed. Also, from 500 °C to 800 °C, the mineral components, including $CoFe_2O_4$ and SBA-15, are not decomposed by temperature rise and only lose a little water, about 4 % (Xiang et al., 2018). However, the SBA-15-GG-*g*-PAA/$CoFe_2O_4$ mesoporous adsorbent showed relatively high thermal resistance with residual weight of 72 % up to 800 °C.

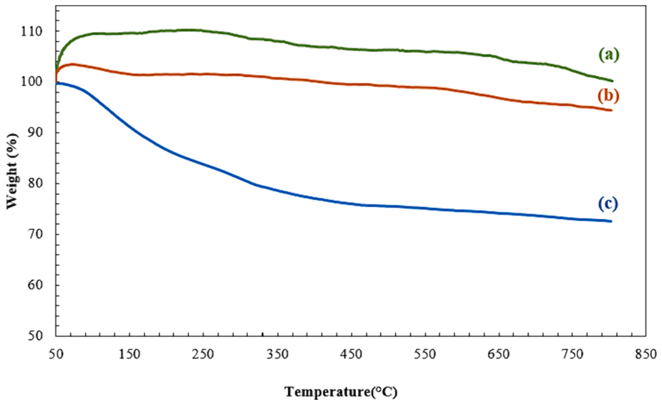

Fig. 6. TGA curves of (a) SBA-15, (b) $CoFe_2O_4$, and (c) SBA-15-GG-*g*-PAA/$CoFe_2O_4$ mesoporous adsorbent.

3.2.6. *X-ray diffraction analysis and small-angle X-ray scattering*

XRD analysis investigates the crystalline phase of the prepared samples. The XRD patterns of $CoFe_2O_4$, GG, SBA-15, GG-*g*-PAA/$CoFe_2O_4$, and SBA-15-GG-*g*-PAA/$CoFe_2O_4$ are represented in Fig. 7. According to the XRD pattern in Fig. 7a, $CoFe_2O_4$ MNPs have cubic phases and no impurities. There are strong reflections from (220), (311), (222), (400), (422), (511), and (440) planes of the f.c.c type lattice of $CoFe_2O_4$. The observed peaks match the position of peaks in their standard diffraction pattern (JCPDS #22–1086). The successful formation of the cubic phase shows the spinel $CoFe_2O_4$ structure, which confirms the FTIR data (Rostami and Shiri, 2020). The presented XRD pattern in Fig. 7b is related to the GG, which exhibits a peak at 19.88°, indicating the peaks of the GG natural polymer (Khan et al., 2020b). Fig. 7c exhibits the SBA-15 XRD pattern, which has a broad peak of amorphous silica centered about $2\theta = 20°$ (Khanh Nguyen et al., 2020). Next, in the XRD pattern of GG-*g*-PAA/$CoFe_2O_4$ (Fig. 7d), the indicative peaks at $2\theta = 10°, 15°, 18°, 20°, 22°, 24°, 25°, 31°, 35°, 47°, 62°$. This pattern also exhibits the presence of $CoFe_2O_4$ MNPs. However, the XRD pattern of SBA-15-GG-*g*-PAA/$CoFe_2O_4$ mesoporous adsorbent in Fig. 7e matches with the distinctive peaks in the previous pattern of GG-*g*-PAA/$CoFe_2O_4$ and the reference pattern of $CoFe_2O_4$, confirming the existence of MNPs in this composite. Also, a relatively broad peak at 20°-28° is only consistent with SBA-15. Still, the decrease in the peak intensity is related to the chemical reaction of grafting PAA with GG polymer onto the cylindrical mesopores of SBA-15. The Small-angle X-ray scattering (SAXS) analysis

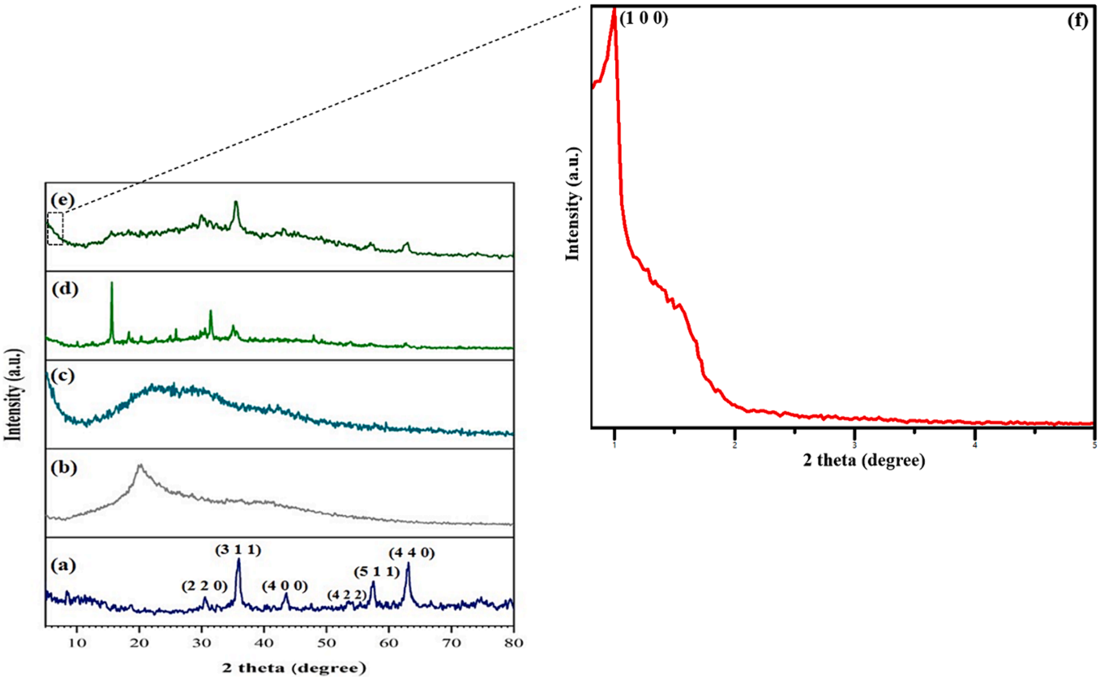

Fig. 7. The XRD patterns of (a) $CoFe_2O_4$, (b) GG, (c) SBA-15, (d) GG-*g*-PAA/$CoFe_2O_4$, (e) SBA-15-GG-*g*-PAA/$CoFe_2O_4$ mesoporous adsorbent, and (f) the SAXS patterns of SBA-15-GG-*g*-PAA/$CoFe_2O_4$ mesoporous adsorbent.

from SBA-15-GG-*g*-PAA/$CoFe_2O_4$ mesoporous confirm the mesoporus structure with characteristic peak related to the SBA-15 The presence of the peak (1 0 0) in the SBA-15-GG-*g*-PAA/$CoFe_2O_4$ spectrum, showed the mesoporous structure.

3.2.7. The N_2 adsorption–desorption isotherm

The specific surface area, pore size, and pore diameter of the prepared SBA-15-GG-*g*-PAA/$CoFe_2O_4$ mesoporous adsorbent were analyzed using BET analysis. Fig. 8 demonstrates the type IV isotherm of SBA-15 with an H1 hysteresis loop, confirming the uniform structure of SBA-15. The N_2 adsorption–desorption isotherm of the SBA-15-GG-*g*-PAA/$CoFe_2O_4$ (type IV isotherm) mesoporous adsorbent reveals a significant decrease in the amount of absorbed N_2 after polymer grafting, indicating the filling or obstruction of the mesopores by the graft polymerization and $CoFe_2O_4$ incorporation. According to the data obtained from the BET analysis, the surface area of SBA-15 was determined to be 686.90 m^2/g. As estimated, the BET surface area of SBA-15 is considerably higher than the surface area of the SBA-15-GG-*g*-PAA/$CoFe_2O_4$. As stated in Table 1, the surface area and pore volume have declined after graft copolymerization of PAA with GG on the SBA-15 substrate and $CoFe_2O_4$ incorporation (Hassanzadeh-Afruzi et al., 2022). Despite the reduced surface area of the SBA-15-GG-*g*-PAA/$CoFe_2O_4$ mesoporous adsorbent compared to a neat SBA-15, its value significantly exceeds that of the sample without SBA-15 inclusion, namely GG-*g*-PAA/$CoFe_2O_4$ (type I isotherm) hydrogel. The wider distribution of pore size in SBA-15-GG-*g*-PAA/$CoFe_2O_4$ mesoporous adsorbent (16.001 nm) compared to the SBA-15 (7.35 nm) can be explained by the incorporation of GG-*g*-PAA/$CoFe_2O_4$ (55.167 nm) into the matrix of the material, which has resulted in structural changes. As a result of the introduction of mesopores as an adsorbent, additional pores may have been created,

Table 1
BET data of SBA-15, GG-*g*-PAA/$CoFe_2O_4$, and SBA-15-GG-*g*-PAA/$CoFe_2O_4$ mesopoures adsorbent.

Sample	Surface area (m^2. g^{-1})	Pore volume (cm^3. g^{-1})	Pore size (nm)
SBA-15	686.90	1.28	7.35
GG-*g*-PAA/$CoFe_2O_4$	1.68	0.023	55.167
SBA-15-GG-*g*-PAA/ $CoFe_2O_4$	40.55	0.162	16.001

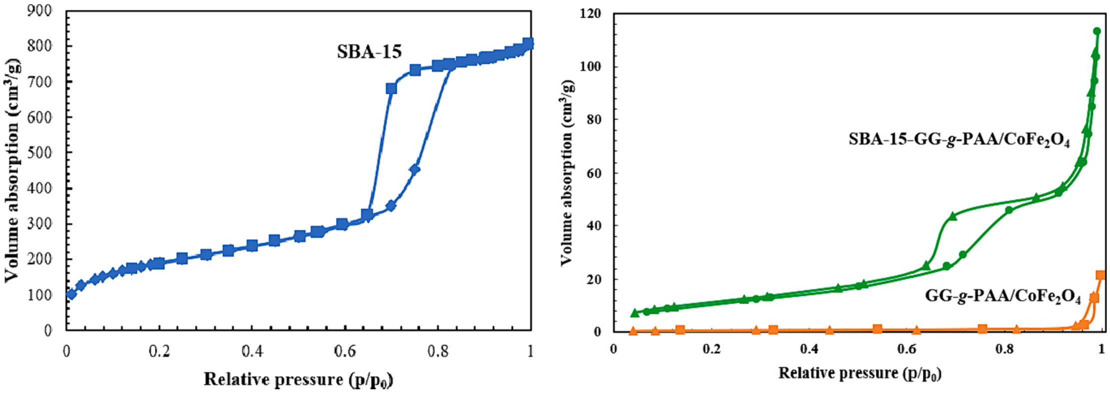

Fig. 8. The isotherm of N_2 adsorption–desorption of SBA-15, GG-*g*-PAA/$CoFe_2O_4$, GG-*g*-PAA/$CoFe_2O_4$ and SBA-15-GG-*g*-PAA/$CoFe_2O_4$ mesoporous adsorbent.

or existing pore sizes and distributions may have been altered. Accordingly, the incorporation of mesoporous adsorbent leads to additional pore size and shape variations in the mesoporous adsorbent. Mesoporous adsorbents may exhibit a more heterogeneous pore size distribution due to GG-g-PAA/$CoFe_2O_4$ presence within the matrix (Kumar et al., 2019; Rafe et al., 2024).

3.2.8. *Zeta potential*

A typical method for quantifying surface potential is the zeta potential. Moreover, it can be used as an indicator to determine the surface charge of a colloidal solution and its stability. Various pH values of 4, 5, 6, 7, 8, and 9 were utilized to study the zeta potential of SBA-15-GG-*g*-PAA/$CoFe_2O_4$ mesoporous adsorbent. HCl and NaOH solutions of 0.1 M concentration were added to adjust the pH of the solution containing the dispersed adsorbent (0.003 g) in an aqueous medium. As a result, the zeta potential was measured three times for each sample, and the results are shown in Fig. 9. Compared to acidic environments, alkaline environments have a negative zeta potential. Because acidic media contain H^+ ions, the negative value of zeta potential is reduced. By deprotonating the structural hydroxyl and carboxylic acid groups, the absolute value of the zeta potential increases with increasing pH. In addition, the SBA-15-GG-*g*-PAA/$CoFe_2O_4$ mesoporous adsorbent has a noticeable negative surface charge, which prevents the mesoporous adsorbent from aggregating at various pH values. A cationic structure of the MG dye results in robust electrostatic interactions with a negative-charged mesoporous adsorbent such as SBA-15-GG-*g*-PAA/$CoFe_2O_4$ mesoporous adsorbent. The zeta potential of the synthesized (SBA-15-GG-*g*-PAA/$CoFe_2O_4$ mesoporous adsorbent at various pHs (4, 5, 6, 7, 8, and 9) mesoporous adsorbent is presented in Table S1 and Fig. 9 (Beigi et al., 2023).

3.3. *Optimizing the effectual factors on the CPF and MG adsorption by SBA-15-GG-g-PAA/$CoFe_2O_4$ mesoporous adsorbent*

3.3.1. *pH of medium*

Different factors, like the reaction medium pH, adsorbent dose, interaction time, and the pollutants' primary concentration, affect pesticide and dye adsorption, so these parameters have to be optimized to obtain the most effective CPF and MG elimination (Mohammed and Ali, 2023; Saharan et al., 2021). At this optimization step, other effectual parameters were assumed constant, including the adsorbent content, interaction time, and primary CPF and MG concentration. The CPF- and MG-containing solution (10.0 mL) was stirred in various pHs (4–9) in 0.01 g of SBA-15-GG-*g*-PAA/$CoFe_2O_4$ adsorbent (30 min) and 100.0 mg/L primary concentration at 25 °C. Afterward, the concentration of the final solution was evaluated by a UV–Vis apparatus. In this regard, the aqueous solution's pH has been altered between 4 and 9 to assess the adsorption effectiveness of CPF and MG on the magnetic SBA-15-GG-*g*-PAA/$CoFe_2O_4$ adsorbent (Fig. 10a). pH is important in the adsorption of MG dye cations from water. In acidic pH, the active sites of SBA-15-GG-*g*-PAA/$CoFe_2O_4$ adsorbent, i.e., hydroxyl groups, become less accessible to MG cations due to protonation at high concentrations of H^+. For this reason, the adsorption capacity observed at acidic pH is low. The adsorption capacity increased with rising pH and reached its highest value at pH 9 and 7 for MG and CPF, with adsorption capacity 96.99 and 99.21 $mg.g^{-1}$, respectively. Considering the non-ionic structure of CPF as an OPP suggests that interactions between the SBA-15-GG-*g*-PAA/$CoFe_2O_4$ adsorbent and CPF molecules are the key binding forces. Therefore, the neutral solution contains the lowest concentrations of protons and hydroxide ions, reducing their ability to inhibit contaminant molecules from binding to the adsorbent. The low concentrations of protons and hydroxide ions in the neutral solution minimize their effects on binding interactions between contaminants and adsorbent active sites. At pH 9, MG cationic dye shows the highest adsorption capacity, which is related to creating a negative charge on the atom (O^-) of the chelating sites of the adsorbent and, as a result of increasing the electrostatic interactions between the adsorbent functional groups and the positively charged MG (N^+) groups. MG generally exists in three forms: chromatic MG, carbinol base, and leuco MG (which decolorizes and precipitates as a carbinol base at pH > 10.5). MG was removed most effectively from local dyeing wastewaters in neutral or alkaline environments (Abubakar et al., 2023).

3.3.2. *Adsorbent dosage*

The adsorbent extent on the sorption capacity was investigated, and its chart is depicted in Fig. 10b. As observed, with the decrease in mesoporous adsorbent amount, the adsorption capacity increases for CPF pesticide and MG dye contaminants. This adsorption capacity increment is related to the rise in the quantity of pollutants available for adsorption on the mesoporous adsorbent unit mass. As a result of the high adsorption capacity of SBA-15-GG-*g*-PAA/$CoFe_2O_4$ at lower mesoporous adsorbent dosages, a large amount of CPF and MB is available for adsorption. As a result of the high quantity of organic pollutants accessible to the mesoporous adsorbent, there is a high adsorption

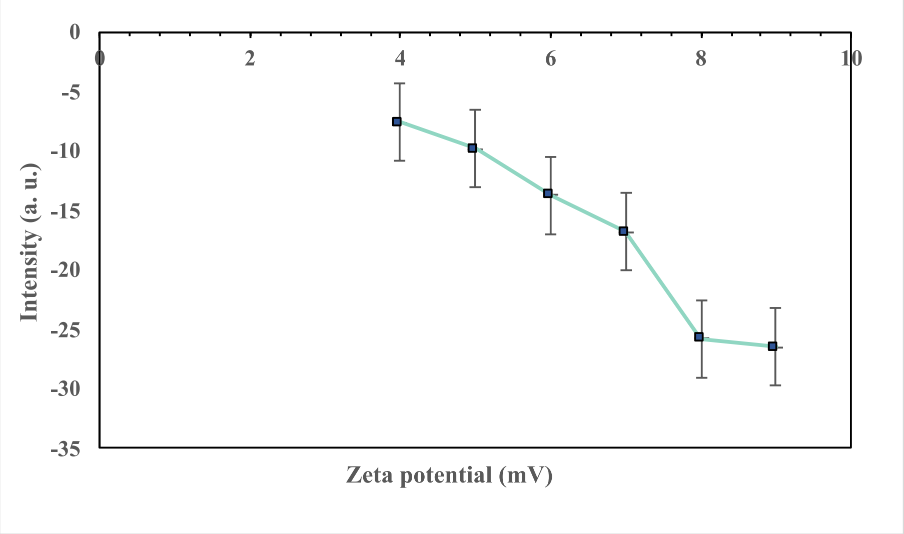

Fig. 9. Zeta potential measurements for the synthesized (SBA-15-GG-*g*-PAA/$CoFe_2O_4$ mesoporous adsorbent at various pH (4, 5, 6, 7, 8, and 9) [the errors (±) represent the relative error values in each case (n = 3)].

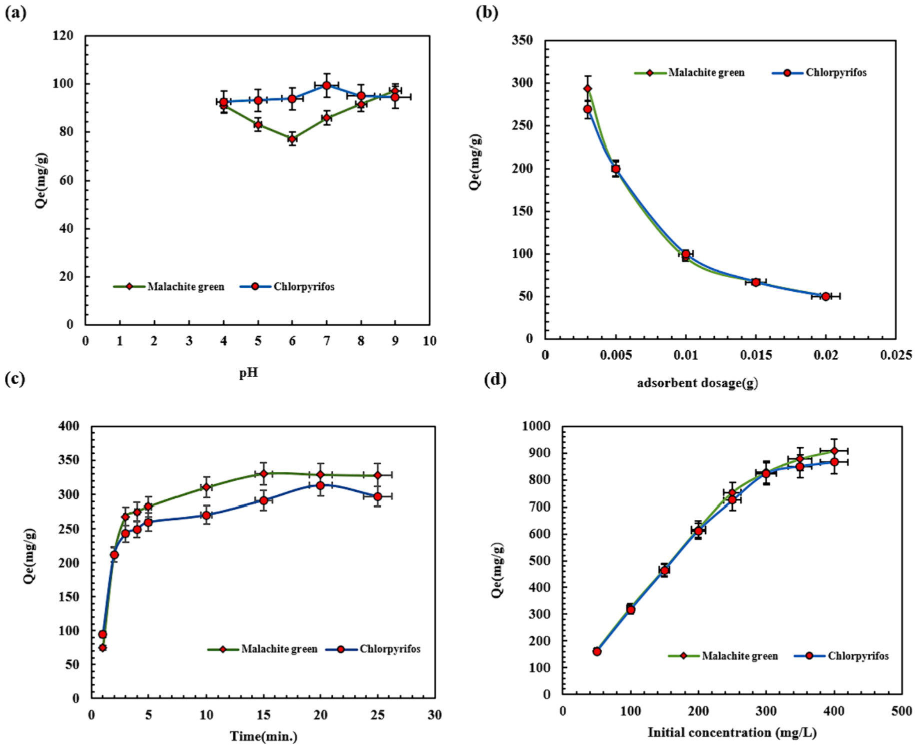

Fig. 10. Effect of (a) solution pH (4–9), (b) adsorbent dosage (0.003–0.02 g), (c) contact time (1–25 min), and (d) initial concentration.

capacity at lower mesoporous adsorbent dosages. Hence, the mesoporous adsorbent molecules' interactions increase, causing the decline in surface adsorption sites and their availability for the contaminant adsorption process. Therefore, using 0.003 g of mesoporous adsorbent, the Q_{max} for CPF and MG was 268.9 mg/g and 293.4 mg/g, respectively. In adsorbent dose optimization, various mesoporous adsorbent amounts (0.003 g, 0.005 g, 0.01 g, 0.015 g, 0.02 g) in the 10.0 mL of a CPF- and MG-containing solution (separately) at a constant primary concentration (100.0 mg/L) and the ideal pH conditions, which is pH 9 and 7 for MG and CPF, respectively, from the pH optimization stage was stirred for 30 min at 25 °C. Ultimately, the final solution concentration was measured (ul Haq et al., 2020).

3.3.3. *Interaction time*

The interaction time is a leading factor in the adsorption with appropriate efficacy, discerning the binding speed and finding the optimum time for removing contaminants, including pesticides and dyes. The contact time (1–25 min) impact on the adsorption of CPF and MG by SBA-15-GG-*g*-PAA/$CoFe_2O_4$ mesoporous adsorbent was investigated at optimum pH and the optimal mesoporous adsorbent amount. As displayed in Fig. 10c, the adsorption capacity of CPF and MG pollutants is elevated with increasing contact time. By increasing the adsorption interaction time, the adsorption capacity of the solution containing CPF pesticide rises up to 20 min and reaches the value of 313.3 mg/g. After that, no noticeable change in the increment of the mesoporous adsorbent's adsorption capacity was observed. Besides, the adsorption capacity of MG dye increased up to 15 min and reached the value of 330.1 mg/g, and then it remained stable. For optimizing time, 10.0 mL of the solution containing CPF pesticide and MG dye at different times (1–25 min), with the optimum dosage of MG by SBA-15-GG-*g*-PAA/$CoFe_2O_4$ mesoporous adsorbent (0.003 g) at 9 and 7 for MG and CPF, respectively, and constant concentration (100.0 mg/L) were contemplated. The optimal time for CPF and MG adsorption was 20 min and 15 min, respectively. The results showed more active sites on the mesoporous adsorbent for interaction with contaminant molecules at first. Nonetheless, these active sites become saturated over time, so no considerable sorption capacity increment is observed (ul Haq et al., 2020).

3.3.4. *Initial pollutant concentration*

The adsorption efficacy was investigated under optimum conditions to test the primary concentration effect on the CPF and MG adsorption rate. Fig. 10d demonstrates a straight relation between the CPF and MG primary concentration and the adsorption capacity. More precisely, by changing the CPF initial concentration from 50.0 mg/L to 400.0 mg/L an increase from 160.4 mg/g to 823.8 mg/g was observed in adsorption capacity and reached its highest level. Moreover, for the MG dye, by changing the initial concentration from 50.0 mg/L to 400.0 mg/L, an increment in the adsorption capacity was detected from 163.3 mg/g to 906.7 mg/g. The optimum CPF pesticide and MG dye concentration is 400.0 mg/L. The CPF and MG initial concentration was obtained for the last optimizing stage as follows: The solution containing CPF and MG (10.0 mL) in various concentrations of 50.0, 100.0, 150.0, 200.0, 250.0, 300.0, 350.0, and 400.0 mg/L with 0.003 g of SBA-15-GG-*g*-PAA/$CoFe_2O_4$ mesoporous adsorbent at the adjusted pH of 9 and 7 for MG and CPF, respectively. The solution was stirred for 15 min for MG and 20 min for CPF, respectively, at 25 °C. Eventually, the concentration was measured (ul Haq et al., 2020).

3.4. *Adsorption isotherm and adsorption kinetics studies*

Until now, the evaluation of how contaminants reach adsorption equilibrium has been explained by various isotherm models such as Freundlich, Langmuir, Temkin, and others. Adsorption isotherms determine the adsorption capacity for CPF and MG and help characterize the surface properties of the mesoporous adsorbent. In this study, the Langmuir and Freundlich isotherms were used to define the adsorption isotherms at equilibrium. Based on statistical thermodynamic laws, the Langmuir isotherm describes the adsorption of a single contaminant layer on the dynamic sites of the mesoporous adsorbent surface. This equation assumes that the active sites on the mesoporous adsorbent surface render similar adsorption energy. On the other hand, the Freundlich isotherm model describes the multilayer adsorption of contaminants on the heterogeneous surface of the mesoporous adsorbent. The equations for the Langmuir and Freundlich models are defined in Eq. (4) and Eq. (5), respectively (Rajahmundry et al., 2021).

$$\frac{C_e}{Q_e} = \frac{1}{K_L Q_{max}} + \frac{1}{Q_{max}} C_e \tag{4}$$

$$LogQ_e = LogK_f + \frac{1}{n} LogC_e \tag{5}$$

In the equations, K_L (L/mg) and K_f (mg/g) are constants for the Langmuir and Freundlich isotherms, respectively. C_e (mg/L) refers to the concentration of the sorbate remaining after reaching equilibrium. Q_e and Q_{max} represent the amounts of CPF and MG contaminant at equilibrium and the maximum pollutant adsorption capacity, respectively, with units of mg/g. The conditions applied for effective adsorption were: initial concentrations of 50–400.0 mg/L for both CPF and MG, pH values of 9 and 7 for MG and CPF, adsorbent amount of 0.003 g, volume (V) of 10.0 mL, contact times of 20 min and 15 min for CPF and MG, temperature (T) of 298 K. Based on these conditions, the adsorption isotherms were evaluated. According to Fig. 11a,b, and the results shown in Table 2, the Langmuir model better describes the CPF adsorption with an R^2 value of 0.9994 compared to 0.9327 for the Freundlich model. This suggests monolayer CPF adsorption on the SBA-15-GG-g-PAA/$CoFe_2O_4$ mesoporous adsorbent surface. The Langmuir and Freundlish R^2 values were 0.9987 and 0.9045 for MG adsorption, indicating MG monolayer adsorption on the prepared mesoporous adsorbent. Overall, the adsorption kinetics process displayed increasing adsorption over time, allowing the rate and mechanism to be assessed. Various kinetic models can describe the kinetics, including pseudo-first-order and pseudo-second-order. The main kinetic models in this study were pseudo-first-order and pseudo-second-order, defined in Eq.6 and Eq.7. (Revellame et al., 2020).

$$\log(Q_e - Q_t) = logQ_e - \frac{k_1}{2.303} t \tag{6}$$

Table 2

Isotherm, kinetic constants, and correlation coefficients for adsorption of CPF and MG on the SBA-15-GG-g-PAA/$CoFe_2O_4$ mesoporous adsorbent.

Model		Parameters	CPF	MG
Isotherm	Freundlich	K_F (mg/g)	165.042	201.301
		N	2.6062	2.848
		R^2	0.9327	0.904
	Langmuir	Q_{max} (mg/g)	909.091	1000
		K_L (L/mg)	0.112	0.131
		R^2	0.9994	0.9987
Kinetics	Pseudo-first-order	k_1 (min^{-1})	0.0893	0.2048
		$Q_{e,exp}$ (mg/g)	313.3	330.066
		$Q_{e,cal}$ (mg/g)	113.647	155.104
		R^2	0.8388	0.9343
	Pseudo-second-order	k_2 (g/mg.min)	0.0023	0.0011
		$Q_{e,exp}$ (mg/g)	313.3	330.067
		$Q_{e,cal}$ (mg/g)	312.5	384.61
		R^2	0.9923	0.9644

$$\frac{t}{Q_t} = \frac{1}{k_2 Q_e^2} + \frac{1}{Q_e} t \tag{7}$$

In the equations, Q_e and Q_t refer to the adsorbed CPF and MG amount in mg/g at the equilibrium state (e) and time (t), respectively. The first-order and second-order rate constants are k_1 (1/min) and k_2 (g/mg. min). The adsorption experiments were conducted over 1–25 min at 25 °C, using 0.003 g of the SBA-15-GG-g-PAA/$CoFe_2O_4$ mesoporous adsorbent in 10.0 mL solutions of 100.0 mg/L concentration for both CPF and MG. The linear plots of adsorption kinetics and associated data for CPF and MG contaminants are shown in Fig. 11c,d, and Table 2. Based on the R^2 values representing the correlation coefficient and difference between experimental and calculated Q_e, the pseudo-second-order kinetic models effectively define the adsorption kinetics for both CPF and MG. These results confirm that chemisorption is the predominant process on the SBA-15-GG-g-PAA/$CoFe_2O_4$ mesoporous adsorbent surface. Additionally, the Q_e values obtained from the pseudo-second-order kinetic model are closer to the equilibrium Q_e than those from

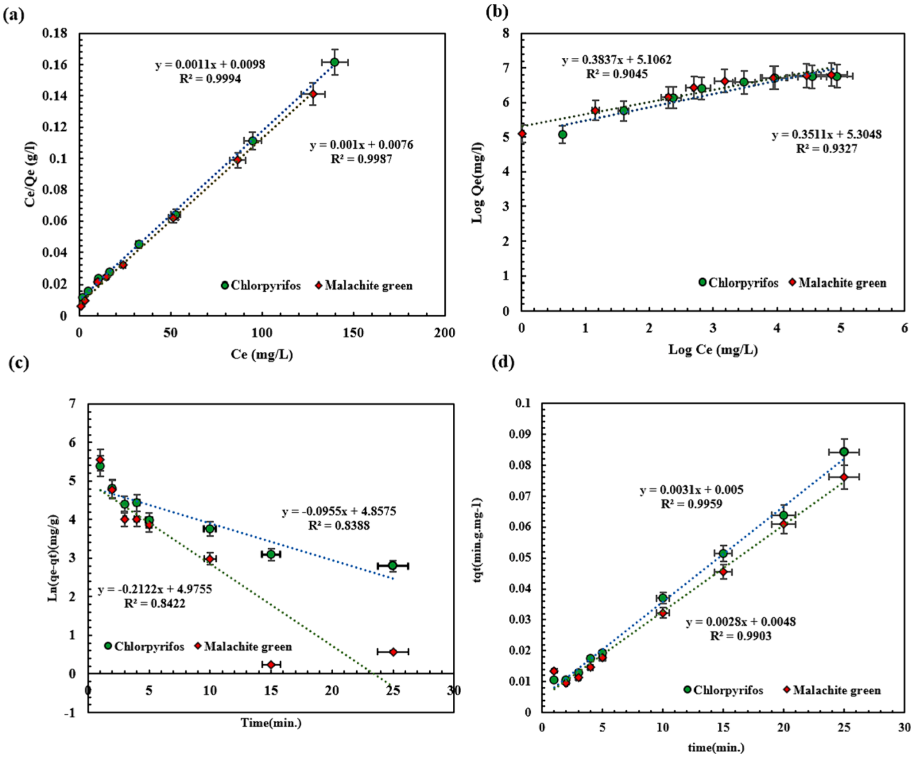

Fig. 11. (a) Langmuir, (b) Freundlich isotherms, (c) pseudo-first order, and (d) pseudo-second-order kinetics.

the pseudo-first-order kinetic model, as seen in Table 2.

A concise comparison has been represented in Table 3 between the CPF and MG's Q_{max} of the SBA-15-GG-*g*-PAA/$CoFe_2O_4$ mesoporous adsorbent and reported adsorbents in previous literature. Based on the reported information, the Q_{max} of the SBA-15-GG-*g*-PAA/$CoFe_2O_4$ mesoporous adsorbent was more improved compared to other adsorbent systems, associated with the enhanced affinity of prepared mesoporous adsorbent's structural and chemical features including an enhanced surface area, porous structure originated from SBA-15 and 3-dimensional hydrogel network, and abundant reactive functional groups, i.e., hydroxyl and carboxyl, interacting with the CPF and MG appropriately. Despite the affordable bioadsorbents (the agricultural substances' residues) than SBA-15-GG-*g*-PAA/$CoFe_2O_4$ mesoporous adsorbent, the removal efficiency of CPF and MG by SBA-15-GG-*g*-PAA/$CoFe_2O_4$ mesoporous adsorbent is higher.

3.5. Recyclability of magnetic SBA-15-GG-g-PAA/$CoFe_2O_4$ mesoporous adsorbent in adsorption/desorption procedure

The adsorbent's retrievability is significant for environmental conservation and decreasing expense, time, and energy since adsorbents rendering such characteristics lessen the issues of the utilized adsorbent elimination and novel adsorbent preparation (Hassanzadeh-Afruzi et al., 2023a; Hassanzadeh-Afruzi et al., 2023c). For the recovery and regeneration investigations of magnetic SBA-15-GG-*g*-PAA/$CoFe_2O_4$ mesoporous adsorbent, three sequential adsorption/desorption cycles were approved. After the CPF and MG adsorption by the magnetic SBA-15-GG-*g*-PAA/$CoFe_2O_4$ mesoporous adsorbent in optimum conditions, the desorption procedure was performed by submerging the mesoporous adsorbent containing CPF in ethanol for 4 h at 25 °C. Also, the desorption of MG-containing mesoporous adsorbent was performed in an HCl solution (0.1 M) at 25 °C. As a consequence, the CPF and MG were released into the mentioned solution, and the SBA-15-GG-*g*-PAA/$CoFe_2O_4$ mesoporous adsorbent was magnetically collected, rinsed with distilled water many times, and dried for further adsorption/desorption tests. As depicted in Fig. 12, after three successive adsorption runs, the adsorption percentage dropped from 82.38 % to 78.92 % and from 82.83 % to 78.61 % for CPF and MG, respectively. The desorption percentage trend was also decreasing from 79.2 % to 73.8 % and from 80.8 % to 75.8 % for CPF and MG, respectively. Based on the obtained results, since the decreasing trend of adsorption/desorption percentage was not considerable, the magnetic SBA-15-GG-*g*-PAA/$CoFe_2O_4$ mesoporous adsorbent is a promising candidate for CPF and MG removal, which can be conveniently separated with no substantial adsorption efficacy decline.

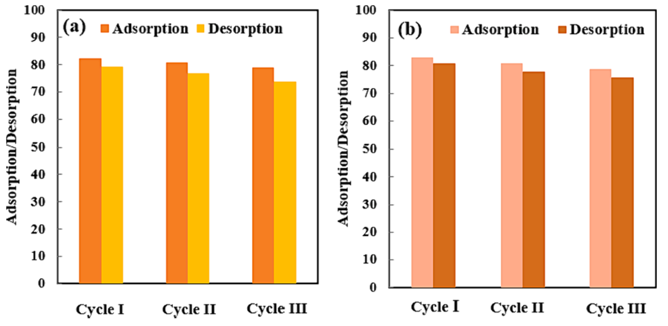

Fig. 12. Reusability of magnetic SBA-15-GG-*g*-PAA/$CoFe_2O_4$ mesoporous adsorbent (a) CPF and (b) MG during three successive runs.

Fig. 13 shows the FT-IR spectra of the reused SBA-15-GG-*g*-PAA/$CoFe_2O_4$ mesoporous adsorbent after three runs. The FT-IR spectra of the recycled SBA-15-GG-*g*-PAA/$CoFe_2O_4$ mesoporous adsorbent showed a comparable absorption to the freshly prepared mesoporous adsorbent, and they are not significantly different from the fresh SBA-15-GG-*g*-PAA/$CoFe_2O_4$ mesoporous adsorbent and all the desired functional groups (significant absorption band at 1000 cm^{-1} related to the Si-O-Si. At 3400 cm^{-1}, there is a strong band associated with OH, and in about 1600 cm^{-1} to 1700 cm^{-1}, the absorption band is associated with grafted with GG, and in the 580 cm^{-1}, the peak is ascribed to Fe – O) are present in the reused CPF, and MG.

3.6. Application to real samples

MG and CPF concentrations were eliminated using the SBA-15-GG-*g*-PAA/$CoFe_2O_4$ mesoporous adsorbent after samples were prepared according to section 2.3.5. Through spiked recovery tests, we determined MG and CPF concentrations in each sample (Table 4). MG and CPF can be accurately determined from different water and industrial samples by the designer of the mesoporous adsorbent based on these satisfactory results (Hassani et al., 2023; Salehi et al., 2024).

3.7. Proposed mechanism of adsorption

According to the articles presented in recent years, we designed a mesoporous adsorbent consisting of a mineral part SBA-15 as a material with an enhanced surface area and uniform pore size, significant thermal stability, a porous structure, and high adsorption ability. SBA-15, with chemical functionality containing well-ordered porosity and reachable active sites, can efficiently interact with organic pollutants. Also, GG, as a natural polymer, significantly promotes the biocompatibility and biodegradability properties of the mesoporous adsorbent. By graft copolymerization of GG with PAA in the SBA-15 substrate, as well as $CoFe_2O_4$ MNPs integration as magnetic components inside this

Table 3
Assessment of the Q_{max} of GG, GG-*g*-PAA/$CoFe_2O_4$, SBA-15, and SBA-15-GG-*g*-PAA/$CoFe_2O_4$ mesoporous adsorbent compared to the previous literature.

Entry	Adsorbent	Qmax (mg/g) For CPF	Ref.	Adsorbent	Qmax (mg/g) For MG	Ref.
1	Magnetic grapheneoxide/N-methyl-glucamine calixarene	93.4	(Nodeh et al., 2019)	Activated carbon/ $CoFe_2O_4$ composites	89.29	(Ai et al., 2010)
2	Fe_3O_4@SiO_2@GO-PEA	32.6	(Wanjeri et al., 2018)	Mesoporous carbon	476.10	(Anbia and Ghaffari, 2011)
3	AGu@mGO(R)	85.47	(Mahdavi et al., 2021)	Zr-SBA-15	140.6	(Ramezani and Zare-Dorabei, 2019)
4	Clay of El-gash river	0.060	(Abdelbagi and Osman, 2018)	SBA-15 NPs	555.0	(Ebrahimpour et al., 2022)
5	Fe_3O_4@SiO_2@GO-PEA (2-phenylethylamine)	25.6	(Wayayi, 2017)	Magnetic hydroxyapatite NPs	208.06	(Hua et al., 2023)
6	GG	53.65	Present work	GG	67.87	Present work
7	GG-*g*-PAA/$CoFe_2O_4$	176.98	Present work	GG-*g*-PAA/$CoFe_2O_4$	194.32	Present work
8	SBA-15	345.61	Present work	SBA-15	321.98	Present work
9	SBA-15-GG-*g*-PAA/$CoFe_2O_4$	909.0909	Present work	SBA-15-GG-*g*-PAA/$CoFe_2O_4$	1000	Present work

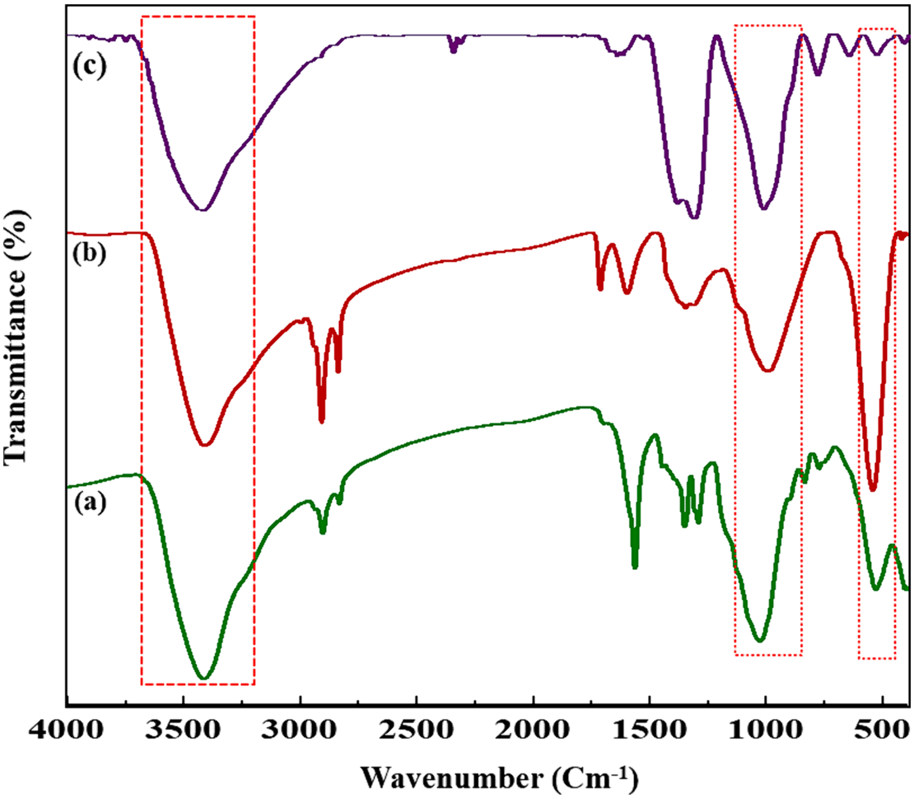

Fig. 13. FT-IR spectra of the fresh SBA-15-GG-g-PAA/$CoFe_2O_4$ mesoporous adsorbent (a), recovered CPF (b), and recovered MG (c).

Table 4
Determination of MG and CPF in various real samples using SBA-15-GG-g-PAA/$CoFe_2O_4$ mesopoures adsorbent.

Sample	Mesoporous adsorbent (mg/L)	Q_{max} (mg.g^{-1}) for MG	Q_{max} (mg.g^{-1}) for CPF
	3120	83.4556.46	42.8829.21
	1129	20.2285.79	16.5557.21
	1833	51.4588.21	56.8871.55
	1417	27.4440.11	13.8851.21
	2724	86.5563.39	53.2174.21
	217	58.6322.94	64.5517.21
	1219	34.7543.37	39.2148.88
	113	33.463.58	36.218.55

polymer matrix, the surface energy of this mesoporous adsorbent expands and also provides more capabilities to bind pollutant molecules. A 3D magnetic hydrogel was created using Borax, which allows the diffusion of the pollutant towards the magnetic SBA-15-GG-g-PAA/$CoFe_2O_4$ mesoporous adsorbent. The prominent interactions between the toxic pollutant and the mesoporous adsorbent are hydrogen bonding, electrostatic attraction, and pore diffusion, as depicted in Fig. 14.

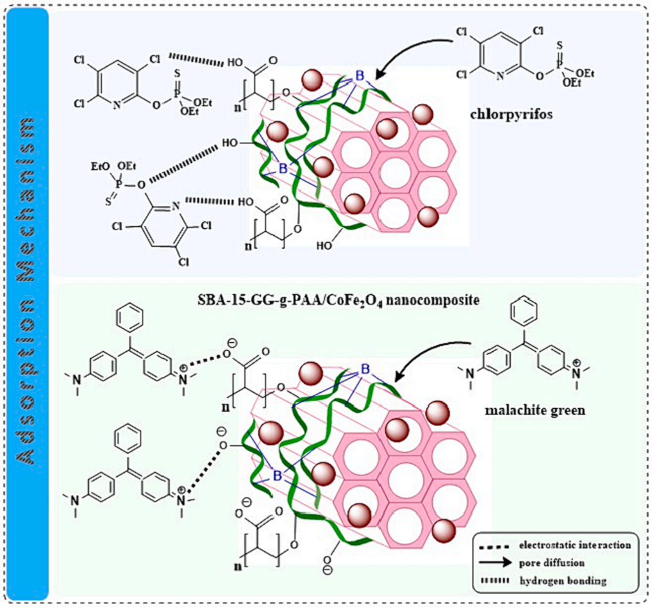

Fig. 14. The adsorption mechanism of CPF and MG on the prepared SBA-15-GG-g-PAA/$CoFe_2O_4$ mesoporous adsorbent.

4. Conclusion

Through various preparation steps, the magnetic SBA-15-GG-g-PAA/$CoFe_2O_4$ mesoporous adsorbent was prepared and used in the CPF and MG elimination. The features of the mesoporous adsorbent were characterized via FTIR, EDX, TGA, SEM, VSM, BET, and XRD analyses. The CPF and MG were efficiently adsorbed by SBA-15-GG-g-PAA/$CoFe_2O_4$ mesoporous adsorbent in the optimal conditions, i.e., (10.0 mL) of solutions containing various concentrations of MG and CPF contaminants (400.0 mg/L) with 0.003 g of SBA-15-GG-g-PAA/$CoFe_2O_4$ mesoporous adsorbent at the adjusted pH of 9 and 7 for MG and CPF, respectively, in 15 min and 20 min reaction time for MG and CPF, respectively. Based on the different analysis results, the prepared mesoporous adsorbent demonstrated enhanced thermal resistance with residual weight of 72 % up to 800 °C and ferromagnetic behavior. The crystallinity and cubic phases of $CoFe_2O_4$ MNPs incorporated in the GG-g-PAA amorphous matrix are confirmed by XRD. FESEM images show $CoFe_2O_4$ MNPs formation, partially aggregated, the GG's smooth and nonporous structure, and the SBA-15′s well-arranged hexagonal structure with cylindrical pores. The presence of SBA-15 substrate in the prepared mesoporous adsorbent has enhanced the BET surface area (40.55 m^2/g of the prepared mesoporous adsorbent compared to composites with no SBA-15. The CPF and MG's Q_{max} at room temperature were 909.0909 mg/g and 1000.0 mg/g, respectively. The obtained information from the adsorption experiments exhibits that the Langmuir model and pseudo-second-order described the isotherm model and adsorption kinetics of CPF and MG adsorption procedure. The hydrogen bonding between the nitrogen and oxygen atoms of the toxic pollutants, viz., CPF and MG, and the electrostatic interaction between MG as a cationic dye and anionic forms of electronegative atom (O^-) of the mesoporous adsorbent is the most significant contaminant-adsorbent interaction. Besides, the magnetic SBA-15-GG-*g*-PAA/$CoFe_2O_4$ mesoporous adsorbent applied to eliminate CPF and MG is isolated and retrieved for three sequential recycling runs without remarkable adsorption efficacy loss. As a result of the excellent adsorption capacity and removal efficiency, as well as reaction stability and recyclability, SBA-15 composites are expected to be applied to pollution remediation in the near future. It is, however, necessary to make some major modifications and developments to achieve these objectives, especially in the following areas: (I) Bicarbonate ions and natural organic matter from wastewater and industrial effluents act as radical scavengers that inhibit the adsorption process. (II) Although nanotechnology has evolved rapidly, sophisticated methods for synthesizing $M - SBA - 15$ catalysts are still necessary for applications beyond the laboratory (M: a transition metal doped within or deposited on the surface of a framework). (III) SBA-15 composite materials are strengthened to ensure their durability and longevity in various industrial settings.

CRediT authorship contribution statement

Mohammad Mehdi Salehi: Writing – original draft. **Kimia Rajabi:** Writing – original draft. **Fereshte Hassanzadeh Afruzi:** Writing – review & editing. **Fatemeh Ganjali:** Writing – review & editing. **Ali Maleki:** Supervision, Writing – review & editing. **Ehsan Nazarzadeh Zare:** Supervision, Writing – original draft.

Declaration of competing interest

The authors declare that they have no known competing financial interests or personal relationships that could have appeared to influence the work reported in this paper.

Acknowledgments

The authors gratefully acknowledge the partial support from the Research Council of Iran University of Science and Technology.

Appendix A. Supplementary data

Supplementary data to this article can be found online at https://doi.org/10.1016/j.arabjc.2024.105751.

References

Abdelbagi, A., Osman, N., 2018. Removal of Chlorpyrifos from aqueous solution by using Clay of El-gash River, Kassala state, Sudan. Univ. Bakht. Alruda Refereed Q Sci. J. 23, 43–57.

Abubakar, H.L., Tijani, J.O., Abdulkareem, A.S., Egbosiuba, T.C., Abdullahi, M., Mustapha, S., Ajiboye, E.A., 2023. Effective removal of malachite green from local dyeing wastewater using zinc-tungstate based materials. Heliyon 9.

Ahmadi, R., Imani, M., Tadjarodi, A., 2020. Microwave assisted synthesis of $CoFe_2O_4$ nanoparticles by utilizing organic promoters and evaluation of its properties. Chem. Proc. 3, 52.

Ai, L., Huang, H., Chen, Z., Wei, X., Jiang, J., 2010. Activated carbon/$CoFe_2O_4$ composites: facile synthesis, magnetic performance and their potential application for the removal of malachite green from water. Chem. Eng. J. 156, 243–249.

Akter, T., Bañuelos, J.L., Andrade, D., Bañuelos, D.I., Saupe, G.B., 2022. Rapid adsorption mechanism of methylene blue onto a porous mixed Ti-Nb oxide. Mater. Chem. Horizons 1, 49–67.

Alazzawi, H.F., Salih, I.K., Albayati, T.M., 2021. Drug delivery of amoxicillin molecule as a suggested treatment for covid-19 implementing functionalized mesoporous SBA-15 with aminopropyl groups. Drug Deliv. 28, 856–864.

Alfonso-Muniozguren, P., Serna-Galvis, E.A., Bussemaker, M., Torres-Palma, R.A., Lee, J., 2021. A review on pharmaceuticals removal from waters by single and combined biological, membrane filtration and ultrasound systems. Ultrason. Sonochem. 76, 105656.

Anbia, M., Ghaffari, A., 2011. Removal of malachite green from dye wastewater using mesoporous carbon adsorbent. J. Iran. Chem. Soc. 8, S67–S76.

Ansari, A., Shahhosseini, S., Maleki, A., 2023. Eco-friendly CO_2 adsorption by activated-nano-clay montmorillonite promoted with deep eutectic solvent. Sep. Sci. Technol. 58, 1252–1274.

Atoub, N., Amiri, A., Badiei, A., Ghasemi, J.B., 2020. Highly selective removal of Pb (II) ions using one-pot thiol-functionalized nanoporous silica with a low amount of directing agent. J. Water Environ. Nanotechnol. 5, 321–330.

Bassyouni, M., Mansi, A., Elgabry, A., Ibrahim, B.A., Kassem, O.A., Alhebeshy, R., 2020. Utilization of carbon nanotubes in removal of heavy metals from wastewater: A review of the CNTs' potential and current challenges. Appl. Phys. A 126, 1–33.

Beigi, P., Ganjali, F., Hassanzadeh-Afruzi, F., Salehi, M.M., Maleki, A., 2023. Enhancement of adsorption efficiency of crystal violet and chlorpyrifos onto pectin hydrogel@Fe_3O_4-bentonite as a versatile nanoadsorbent. Sci. Rep. 13, 10764.

Boulahbal, M., Malouki, M.A., Canle, M., Redouane-Salah, Z., Devanesan, S., AlSalhi, M. S., Berkani, M., 2022. Removal of the industrial azo dye crystal violet using a natural clay: Characterization, kinetic modeling, and RSM optimization. Chemosphere 306, 135516.

Dindar, M.H., Yaftian, M.R., Hajihasani, M., Rostamnia, S., 2016. Refinement of contaminated water by Cr (VI), As (V) and Hg (II) using N-donor ligands arranged on SBA-15 platform; batch and fixed-bed column methods. J. Taiwan Inst. Chem. Eng. 67, 325–337.

Dolatyari, L., Yaftian, M.R., Rostamnia, S., 2016a. Adsorption characteristics of Eu (III) and Th (IV) ions onto modified mesoporous silica SBA-15 materials. J. Taiwan Inst. Chem. Eng. 60, 174–184.

Dolatyari, L., Yaftian, M.R., Rostamnia, S., 2016b. Removal of uranium (VI) ions from aqueous solutions using Schiff base functionalized SBA-15 mesoporous silica materials. J. Environ. Manag. 169, 8–17.

Dolatyari, L., Yaftian, M.R., Rostamnia, S., 2017a. Fixed-bed column dynamic studies and breakthrough curve analysis of Eu (III) ion adsorption onto chemically modified SBA-15 silica materials. Sep. Sci. Technol. 52, 393–403.

Dolatyari, L., Yaftian, M.R., Rostamnia, S., Seyeddorraji, M.S., 2017b. Multivariate optimization of a functionalized SBA-15 mesoporous based solid-phase extraction for U (VI) determination in water samples. Anal. Sci. 33, 769–776.

Dolatyari, L., Yaftian, M.R., Rostamnia, S., 2018. Adsorption of Th (IV) and U (VI) on functionalized SBA-15 mesoporous silica materials using fixed bed column method; breakthrough curves prediction and modeling. Sep. Sci. Technol. 53, 1282–1294.

Dolatyari, L., Shateri, M., Yaftian, M.R., Rostamnia, S., 2019. Unmodified SBA-15 adsorbents for the removal and separation of Th (IV) and U (VI) ions: the role of pore channels and surface-active sites. Sep. Sci. Technol. 54, 2863–2878.

Duan, C., Ma, T., Wang, J., Zhou, Y., 2020. Removal of heavy metals from aqueous solution using carbon-based adsorbents: A review. J. Water Proc. Eng. 37, 101339.

Dulski, M., Laskowska, M., Sułowicz, S., Krzykawski, T., Pastukh, O., Zieliński, P., Pawlik, P., Nowak, A., 2020. The impact of the functionalization of silica mesopores on the structural and biological features of SBA-15. Microporous Mesoporous Mater. 306, 110453.

Dutta, K., Das, B., Mondal, D., Adhikari, A., Rana, D., Chattopadhyay, A.K., Banerjee, R., Mishra, R., Chattopadhyay, D., 2017. An ex situ approach to fabricating nanosilica reinforced polyacrylamide grafted guar gum nanocomposites as an efficient biomaterial for transdermal drug delivery application. New J. Chem. 41, 9461–9471.

Ebrahimpour, M., Hassaninejad-Darzi, S.K., Zavvar Mousavi, H., 2022. Adsorption of ternary toxic crystal violet, malachite green and methylene blue onto synthesised SBA-15 mesoporous nanoparticles. Int. J. Environ. Anal. Chem. 102, 2512–2535.

Farajzadeh, M., Alamgholiloo, H., Nasibipour, F., Banaei, R., Rostamnia, S., 2020. Anchoring Pd-nanoparticles on dithiocarbamate-functionalized SBA-15 for hydrogen generation from formic acid. Sci. Rep. 10, 18188.

Farrag, M., 2022. Electrostatic adsorption of ultra-small silver nanoclusters on titanium dioxide modified mesoporous MCM-41as a high-performance photocatalyst for wastewater treatment. J. Photochem. Photobiol. a: Chem. 422, 113551.

Gámez, E., Elizondo-Castillo, H., Tascon, J., García-Salinas, S., Navascues, N., Mendoza, G., Arruebo, M., Irusta, S., 2020. Antibacterial effect of thymol loaded SBA-15 nanorods incorporated in PCL electrospun fibers. Nanomaterials 10, 616.

Gihar, S., Kumar, D., Kumar, P., 2021. Facile synthesis of novel pH-sensitive grafted guar gum for effective removal of mercury (II) ions from aqueous solution. Carbohydr. Polym. Technol. Appl. 2, 100110.

Gil, A., Santamaría, L., Korili, S., Vicente, M., Barbosa, L., De Souza, S., Marçal, L., De Faria, E., Ciuffi, K., 2021. A review of organic-inorganic hybrid clay based adsorbents for contaminants removal: Synthesis, perspectives and applications. J. Environ. Chem. Eng. 9, 105808.

Hajizadeh, Z., Salehi, M.M., 2023. MOFs Bandstructure, Physicochemical Aspects of Metal-Organic Frameworks: A New Class of Coordinative Materials. Springer, pp. 79–90.

Hassani, F., Larki, A., Ghomi, M., Pourreza, N., 2023. Gold nanoparticles embedded Fe-BTC (AuNPs@Fe-BTC) metal-organic framework as a fluorescence sensor for the selective detection of As (III) in contaminated waters. Spectrochim. Acta A Mol. Biomol. Spectrosc. 302, 123104.

Hassanzadeh-Afruzi, F., Esmailzadeh, F., Asgharnasl, S., Ganjali, F., Taheri-Ledari, R., Maleki, A., 2022. Efficient removal of Pb (II)/Cu (II) from aqueous samples by a guanidine-functionalized SBA-15/Fe3O4. Sep. Purif. Technol. 291, 120956.

Hassanzadeh-Afruzi, F., Ranjbar, G., Salehi, M.M., Esmailzadeh, F., Maleki, A., 2023a. Thiacalix [4] arene-functionalized magnetic xanthan gum (TC4As-XG@Fe3O4) as a hydrogel adsorbent for removal of dye and pesticide from water medium. Sep. Purif. Technol. 306, 122700.

Hassanzadeh-Afruzi, F., Salehi, M.M., Heidari, G., Maleki, A., Zare, E.N., 2023b. Hydrolyzed Arabic gum-grafted-polyacrylonitrile@zinc ferrite nanocomposite as an efficient biocatalyst for the synthesis of pyranopyrazoles derivatives. J. Mol. Struct. 1274, 134490.

Hassanzadeh-Afruzi, F., Salehi, M.M., Ranjbar, G., Esmailzadeh, F., Hanifehnejad, P., Azizi, M., Eshrati yeganeh, F., Maleki, A., 2023c. Utilizing magnetic xanthan gum nanocatalyst for the synthesis of acridindion derivatives via functionalized macrocycle Thiacalix[4]arene. Sci. Rep. 13, 22162.

Hua, Y., Xu, D., Liu, Z., Zhou, J., Han, J., Lin, Z., Xu, D., Chen, G., Huang, X., Chen, J., 2023. Effective adsorption and removal of malachite green and Pb2 + from aqueous samples and fruit juices by pollen–inspired magnetic hydroxyapatite nanoparticles/hydrogel beads. J. Clean. Prod. 411, 137233.

Kanwal, S., Irfan, A., Al-Hussain, S.A., Sharif, G., Mumtaz, A., Batool, F., Zaki, M.E., 2023. Fabrication of composites of sodium alginate with guar gum and iron coated activated alumina for the purification of water from direct blue 86. Coatings 13, 103.

Khan, N., Kumar, D., Kumar, P., 2020b. Silver nanoparticles embedded guar gum/gelatin nanocomposite: green synthesis, characterization and antibacterial activity. Colloids Interface Sci. Commun. 35, 100242.

Khan, M.U.A., Raza, M.A., Razak, S.I.A., Abdul Kadir, M.R., Haider, A., Shah, S.A., Mohd Yusof, A.H., Haider, S., Shakir, I., Aftab, S., 2020a. Novel functional antimicrobial and biocompatible arabinoxylan/guar gum hydrogel for skin wound dressing applications. J. Tissue Eng. Regen. Med. 14, 1488–1501.

Khanh Nguyen, Q.N., Yen, N.T., Hau, N.D., Tran, H.L., 2020. Synthesis and characterization of mesoporous silica SBA-15 and ZnO/SBA-15 photocatalytic materials from the ash of brickyards. J. Chem. 2020, 1–8.

Kim, J.Y., Atique, U., Mamun, M., An, K.-G., 2021. Long-term interannual and seasonal links between the nutrient regime, sestonic chlorophyll and dominant bluegreen algae under the varying intensity of monsoon precipitation in a drinking water reservoir. Int. J. Environ. Res. Public Health 18, 2871.

Kobayashi, Y., Ogata, F., Nakamura, T., Kawasaki, N., 2020. Synthesis of novel zeolites produced from fly ash by hydrothermal treatment in alkaline solution and its evaluation as an adsorbent for heavy metal removal. J. Environ. Chem. Eng. 8, 103687.

Kumar, P.S., Korving, L., Keesman, K.J., van Loosdrecht, M.C., Witkamp, G.-J., 2019. Effect of pore size distribution and particle size of porous metal oxides on phosphate adsorption capacity and kinetics. Chem. Eng. J. 358, 160–169.

Liou, T.-H., Chen, G.-W., Yang, S., 2022. Preparation of amino-functionalized mesoporous SBA-15 nanoparticles and the improved adsorption of tannic acid in wastewater. Nanomaterials 12, 791.

Liu, F., Wang, A., Xiang, M., Hu, Q., Hu, B., 2022. Effective adsorption and immobilization of Cr (VI) and U (VI) from aqueous solution by magnetic amine-functionalized SBA-15. Sep. Purif. Technol. 282, 120042.

Mahdavi, V., Taghadosi, F., Dashtestani, F., Bahadorikhalili, S., Farimani, M.M., Ma'mani, L., Khaneghah, A.M., 2021. Aminoguanidine modified magnetic graphene oxide as a robust nanoadsorbent for efficient removal and extraction of chlorpyrifos residue from water. J. Environ. Chem. Eng. 9, 106117.

Makhado, E., Motshabi, B.R., Allouss, D., Ramohlola, K.E., Modibane, K.D., Hato, M.J., Jugade, R.M., Shaik, F., Pandey, S., 2022. Development of a ghatti gum/poly (acrylic acid)/TiO2 hydrogel nanocomposite for malachite green adsorption from aqueous media: Statistical optimization using response surface methodology. Chemosphere 306, 135524.

Marjanian, M.M., Shahhosseini, S., Ansari, A., 2021. Investigation of the ultrasound assisted CO_2 absorption using different absorbents. Process Saf. Environ. Prot. 149, 277–288.

Mohammed, A.A., Ali, D.K., 2023. Bentonite-layered double hydroxide composite as potential adsorbent for removal of Abamectin pesticide from wastewater. Results Surf. Interfaces 100099.

Najafi, H., Farajfaed, S., Zolgharnian, S., Mirak, S.H.M., Asasian-Kolur, N., Sharifian, S., 2021. A comprehensive study on modified-pillared clays as an adsorbent in wastewater treatment processes. Process Saf. Environ. Prot. 147, 8–36.

Nakhjiri, M.T., Marandi, G.B., Kurdtabar, M., 2021. Preparation of magnetic double network nanocomposite hydrogel for adsorption of phenol and p-nitrophenol from aqueous solution. J. Environ. Chem. Eng. 9, 105039.

Nandhini, A., Harshiny, M., Gummadi, S.N., 2021. Chlorpyrifos in environment and food: a critical review of detection methods and degradation pathways. Environ. Sci.: Process. Impacts 23, 1255–1277.

Nasrollahzadeh, M., Sajjadi, M., Iravani, S., Varma, R.S., 2021. Starch, cellulose, pectin, gum, alginate, chitin and chitosan derived (nano) materials for sustainable water treatment: A review. Carbohydr. Polym. 251, 116986.

Nguyen, V.C., Huynh, T.K.N., 2014. Reusable nanocomposite of CoFe2O4/chitosan-graft-poly (acrylic acid) for removal of Ni (II) from aqueous solution. Adv. Nat. Sci.: Nanosci. Nanotechnol. 5, 025007.

Nodeh, H.R., Kamboh, M.A., Ibrahim, W.A.W., Jume, B.H., Sereshti, H., Sanagi, M.M., 2019. Equilibrium, kinetic and thermodynamic study of pesticides removal from water using novel glucamine-calix [4] arene functionalized magnetic graphene oxide. Environ. Sci.: Process. Impacts 21, 714–726.

Rafe, M.H., Shahzad, K., Josien, L., Bonne, M., Mohsenzadeh, E., Delaite, C., Lebeau, B., Khubaib, M.A., Adolphe, D.C., 2024. Structure-Property Behavior of Nanofibers Based on Polyacrylonitrile/Mesoporous Silica (SBA-15) Composites Prepared by Electrospinning. Arab. J. Sci. Eng. 49, 1245–1256.

Rajahmundry, G.K., Garlapati, C., Kumar, P.S., Alwi, R.S., Vo, D.-V.-N., 2021. Statistical analysis of adsorption isotherm models and its appropriate selection. Chemosphere 276, 130176.

Ramezani, F., Zare-Dorabei, R., 2019. Simultaneous ultrasonic-assisted removal of malachite green and methylene blue from aqueous solution by Zr-SBA-15. Polyhedron 166, 153–161.

Revellame, E.D., Fortela, D.L., Sharp, W., Hernandez, R., Zappi, M.E., 2020. Adsorption kinetic modeling using pseudo-first order and pseudo-second order rate laws: A review. Clean. Eng. Technol. 1, 100032.

Rostami, H., Shiri, L., 2020. CoFe2O4@SiO2-PA-CC-guanidine nanoparticles: A novel, efficient, and recyclable catalyst for the synthesis of 3, 5-disubstituted-2, 6-dicyanoaniline derivatives. Appl. Organomet. Chem. 34, e5599.

Sadeghi, M., Moradian, M., Tayebi, H.-A., Mirabi, A., 2023. Removal of Penicillin G from aqueous medium by PPI@SBA-15/ZIF-8 super adsorbent: Adsorption isotherm, thermodynamic, and kinetic studies. Chemosphere 311, 136887.

Saharan, P., Kumar, V., Mittal, J., Sharma, V., Sharma, A.K., 2021. Efficient ultrasonic assisted adsorption of organic pollutants employing bimetallic-carbon nanocomposites. Sep. Sci. Technol. 56, 2895–2908.

Salehi, M.M., Hassanzadeh-Afruzi, F., Heidari, G., Maleki, A., Zare, E.N., 2023a. In situ preparation of MOF-199 into the carrageenan-grafted-polyacrylamide@Fe_3O_4 matrix for enhanced adsorption of levofloxacin and cefixime antibiotics from water. Environ. Res. 233, 116466.

Salehi, M.M., Hassanzadeh-Afruzi, F., Heidari, G., Maleki, A., Zare, E.N., 2023b. In situ preparation of MOF-199 into the carrageenan-grafted-polyacrylamide@Fe_3O_4 matrix for enhanced adsorption of levofloxacin and cefixime antibiotics from water. Environ Res. 116466.

Salehi, M.M., Hassanzadeh-Afruzi, F., Esmailzadeh, F., Choopani, L., Rajabi, K., Kuzekanan, H.N., Azizi, M., Demchuk, O.M., Maleki, A., 2024. Chlorpyrifos and diazinon elimination through pAAm-g-XG/HKUST-1@Fe_3O_4 biopolymer nanoadsorbent hydrogel from wastewater: Preparation, characterization, kinetics and isotherm. Sep. Purif. Technol. 334, 126097.

Saraf, P., Montazer, M., 2023. Extraction, structural properties, and applications of guar gum. Natural Gums. Elsevier 185–260.

Sedaghati, N., Habibi-Yangjeh, A., Asadzadeh-Khaneghah, S., Ghosh, S., 2021. Photocatalytic performance of oxygen vacancy rich-TiO2 combined with Bi4O5Br 2 nanoparticles on degradation of several water pollutants. Adv. Powder Technol. 32, 304–316.

Sivagurunathan, P., Gibin, S., 2016. Preparation and characterization of nanosized cobalt ferrite particles by co-precipitation method with citrate as chelating agent. J. Mater. Sci.: Mater. Electron. 27, 8891–8898.

ul Haq, A., Saeed, M., Usman, M., Naqvi, S.A.R., Bokhari, T.H., Maqbool, T., Ghaus, H., Tahir, T., Khalid, H., 2020. Sorption of chlorpyrifos onto zinc oxide nanoparticles impregnated Pea peels (Pisum sativum L): Equilibrium, kinetic and thermodynamic studies. Environ. Technol. Innov. 17, 100516.

Upadhyay, U., Sreedhar, I., Singh, S.A., Patel, C.M., Anitha, K., 2021. Recent advances in heavy metal removal by chitosan based adsorbents. Carbohydr. Polym. 251, 117000.

Vishwas, M., Babu, K.V., Gowda, K.A., Gandla, S.B., 2022. Synthesis, characterization and photo-catalytic activity of magnetic CoFe2O4 nanoparticles prepared by temperature controlled co-precipitation method. Mater. Today: Proc. 68, 497–501.

Wang, L., Shi, C., Pan, L., Zhang, X., Zou, J.-J., 2020. Rational design, synthesis, adsorption principles and applications of metal oxide adsorbents: a review. Nanoscale 12, 4790–4815.

Wang, J., Zhang, J., Han, L., Wang, J., Zhu, L., Zeng, H., 2021. Graphene-based materials for adsorptive removal of pollutants from water and underlying interaction mechanism. Adv. Colloid Interface Sci. 289, 102360.

Wanjeri, V., Sheppard, C., Prinsloo, A., Ngila, J., Ndungu, P., 2018. Isotherm and kinetic investigations on the adsorption of organophosphorus pesticides on graphene oxide based silica coated magnetic nanoparticles functionalized with 2-phenylethylamine. J. Environ. Chem. Eng. 6, 1333–1346.

Wayayi, V.W.O., 2017. Nanocarbon Anchored on Magnetic Iron Oxide-Silica Core Shell Nanocomposite for Extraction of Organophosphate Pesticides from Natural Water. University of Johannesburg (South Africa).

Wu, H., Xiao, Y., Guo, Y., Miao, S., Chen, Q., Chen, Z., 2020. Functionalization of SBA-15 mesoporous materials with 2-acetylthiophene for adsorption of Cr (III) ions. Microporous Mesoporous Mater. 292, 109754.

Xiang, X., Suo, H., Xu, C., Hu, Y., 2018. Covalent immobilization of lipase onto chitosan-mesoporous silica hybrid nanomaterials by carboxyl functionalized ionic liquids as the coupling agent. Colloids Surf. B Biointerfaces 165, 262–269.

Yadav, S., Yadav, A., Bagotia, N., Sharma, A.K., Kumar, S., 2021. Adsorptive potential of modified plant-based adsorbents for sequestration of dyes and heavy metals from wastewater-A review. J. Water Proc. Eng. 42, 102148.

Yousofvand, Z., Hajjami, M., Ghorbani, F., Ghafouri-Nejad, R., 2018. Synthesis of Ni (II)-3, 5-dichloro-2-hydroxybenzenesulfonyl chloride supported SBA-15 and its application as a nanoreactor catalyst for the synthesis of diaryl sulfides via reaction of aryl halides with thiourea or S8. J. Porous Mater. 25, 1349–1358.

Zanele, Z.P., Mtunzi, F.M., Nelana, S.M., Ebelegi, A.N., Ayawei, N., Dikio, E.D., Wankasi, D., Diagboya, P.N., 2021. Metals and antibiotics as aqueous sequestration targets for magnetic polyamidoamine-grafted SBA-15. Langmuir 37, 9764–9773.